

Shotgun crystal structure prediction using machine-learned formation energies

Chang Liu¹, Hiromasa Tamaki², Tomoyasu Yokoyama², Kensuke Wakasugi², Satoshi Yotsuhashi², Minoru Kusaba¹, and Ryo Yoshida^{1,3,4,*}

¹The Institute of Statistical Mathematics, Research Organization of Information and Systems, Tachikawa, Tokyo 190-8562, Japan

²Technology Division, Panasonic Holdings Corporation, Kadoma, Osaka 571-8508, Japan

³National Institute for Materials Science, Research and Service Division of Materials Data and Integrated System, Tsukuba, 305-0047, Japan

⁴The Graduate University for Advanced Studies, Department of Statistical Science, Tachikawa, 190-8562, Japan

*yoshidar@ism.ac.jp

ABSTRACT

Stable or metastable crystal structures of assembled atoms can be predicted by finding the global or local minima of the energy surface with respect to the atomic configurations. Generally, this requires repeated first-principles energy calculations that are impractical for large systems, such as those containing more than 30 atoms in the unit cell. Here, we have made significant progress in solving the crystal structure prediction problem with a simple but powerful machine-learning workflow; using a machine-learning surrogate for first-principles energy calculations, we performed non-iterative, single-shot screening using a large library of virtually created crystal structures. The present method relies on two key technical components: transfer learning, which enables a highly accurate energy prediction of pre-relaxed crystalline states given only a small set of training samples from first-principles calculations, and generative models to create promising and diverse crystal structures for screening. Here, first-principles calculations were performed only to generate the training samples, and for the optimization of a dozen or fewer finally narrowed-down crystal structures. Our shotgun method was more than 5–10 times less computationally demanding and achieved an outstanding prediction accuracy that was 2–6 times higher than that of the conventional methods that rely heavily on iterative first-principles calculations.

Introduction

Predicting the stable or metastable structures of a crystalline system with a given chemical composition is a fundamental unsolved problem that has been studied for several decades in solid-state physics^{1,2}. In principle, the stable or metastable crystal structures of assembled atoms or molecules in the solid state can be determined using quantum mechanical calculations. Crystal structure prediction (CSP) is based on finding the global or local minima of the energy surface defined on a broad space of atomic configurations, in which the energy can be evaluated by first-principles density functional theory (DFT) calculations. To solve the CSP problem, we can apply an exploratory algorithm to determine the crystal structure at the global or local minimum by successively displacing the atomic configurations along the energy gradient.

To solve this hard problem, a broad array of CSP methods have been developed to date, including brute-force random search^{3–5}, simulated annealing^{6,7}, the Wang-Landau method⁸, particle swarm optimization^{9,10}, genetic algorithms^{2,11,12}, Bayesian optimization¹³, and look ahead based on quadratic approximation (LAQA)¹⁴. More recently, machine learning interatomic potentials have been attracting increasing attention because they can greatly speed up the optimization process by bypassing time-consuming *ab initio* calculations^{15,16}. Conventionally, genetic manipulations such as mutation and crossover are performed to modify a current set of candidate crystal structures, and their DFT energies are used then as goodness-of-fit scores to prioritize promising candidates for survival in the new generation. This process is repeated until the energy minima are reached. For example, the pioneering software package USPEX implements

a comprehensive set of genetic operations such as the mutation and crossover of crystal objects^{2,11,12}, while the CALYPSO code employs a genetic operation called the swarm shift¹⁷. However, such algorithms are time-consuming because of the need to perform ab initio structural relaxation of the candidate crystals at every step of the optimization process. CrySPY was developed to increase the computational efficiency by introducing a machine-learning energy calculator¹⁴ based on the Gaussian process regressor¹⁸. The predictive performance is successively improved by accumulating a training set of candidate crystal structures and their relaxed energies via Bayesian optimization¹⁹. The surrogate energy calculation model efficiently rules out unpromising candidates whose energies are unlikely to reach the minima. However, most existing methods utilize relaxed energy values to evaluate the goodness-of-fit in the selection process or to produce instances to train a surrogate model. Therefore, it is necessary to relax all candidate structures at every step of the sequential search. It is clear that such methods are impractical for large systems that contain more than 30–40 atoms in a unit cell, owing to their enormous computational cost. Furthermore, the predictive capability of this approach is much lower than expected regardless of the system size, as will be demonstrated by the comprehensive test shown later.

To overcome this difficulty, a promising solution is to fully replace ab initio energy calculations with machine-learning surrogates. Energy prediction models trained using DFT property databases, such as the Materials Project^{20,21}, AFLOW^{22,23}, and OQMD^{24,25}, have been reported to exhibit a quite high prediction accuracy^{26–28}. However, models trained on the instances from stable or metastable structures in such a database are inapplicable to the prediction of unrelaxed energies of varying atomic configurations for a given target system. Such models can predict energy differences between different crystalline systems but lack the ability to quantitatively discriminate energy differences of distinct conformations for the system of interest. This is the ability that is required for solving the CSP problem.

In this study, we employed a simple approach to building a predictive model for formation energies. First, a crystal-graph convolutional neural network (CGCNN)²⁸ was trained using diverse crystals with stable or metastable state energies from the Materials Project database. Subsequently, for a given chemical composition as the target, the DFT energies of a few dozen randomly generated unrelaxed structures were calculated by performing single-point energy calculations, and a transfer learning technique^{29,30} was applied to fine-tune the pretrained CGCNN to the target system. Generally, limited data are available for model training, and randomly generated crystal conformations are distributed in high-energy regions. Models trained on such data that are biased towards high-energy states are generally not applicable to the extrapolative domain of low-energy states in which optimal or suboptimal conformers exist. In CSP, a surrogate model must be able to predict the energy of various conformations with high- to low-energy states corresponding to the pre- and post-relaxed crystal structures, respectively. We demonstrate that the surrogate model derived using the transfer learning method exhibited sufficiently high prediction accuracy, even in the domain of low-energy states.

After creating candidate crystal structures, exhaustive virtual screening was performed using the transferred energy predictor. The narrowed-down candidate crystals were relaxed by performing DFT calculations. Currently, a wide variety of structure generators can be applied to generate the virtual crystal libraries, e.g., (i) methods based on element substitution using existing crystal structures as templates^{31–33}, (ii) atomic coordinate generators that take into account crystallographic topology and symmetry^{34,35}, (iii) algorithms for reconstructing atomic configurations based on interatomic distance matrices (contact maps) predicted by machine learning³⁶, and (iv) deep generative models that mimic crystals synthesized to date^{37–39}. In this study, we validated our framework using two sets of virtual libraries created using methods related to (i) and (ii). Our workflow, which can be regarded as a high-throughput virtual screening of crystal structures, is perhaps the simplest among existing CSP methods to date. In the entire workflow, first-principles single-point calculations were performed for approximately 1,000 structures to create a training set for the transferred energy predictor and for the structural relaxation of a dozen or fewer narrowed-down candidate crystals in the final stage. Compared to conventional methods such as USPEX, the present method is 5–10 times less computationally demanding. Furthermore, the prediction accuracy is greatly improved compared to the existing methods; in the prediction of the stable structures of 90 benchmark crystals that were chosen to obtain a set of materials with diverse space groups, structure types, constituent elements, system sizes, and application domains, we succeeded in accurately predicting 84.4% of structures. This prediction accuracy is 2–6 times higher than that of USPEX; furthermore, the proposed method rapidly predicted stable structures with low symmetry or with unit cells containing many atoms that could not be predicted correctly by USPEX.

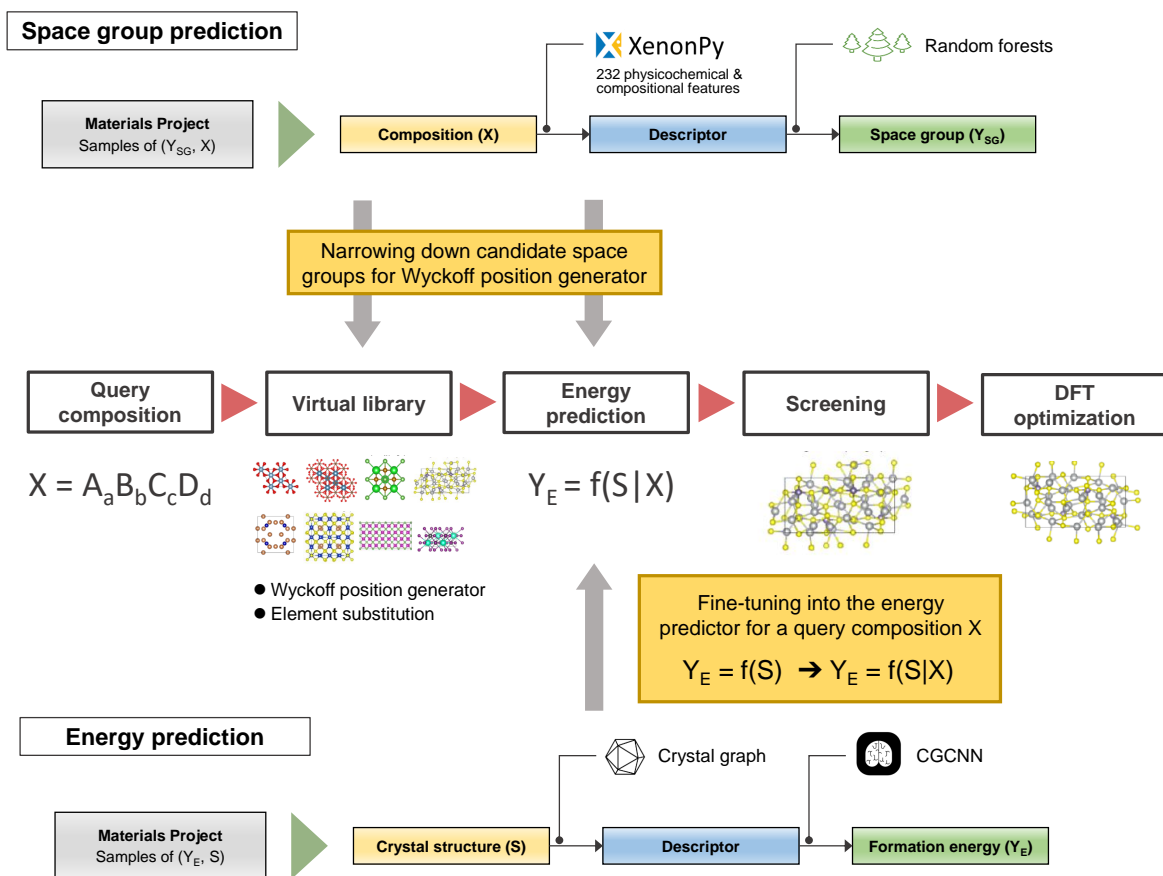


Figure 1. Workflow of the shotgun crystal structure prediction based on the virtual screening using machine-learned formation energies.

Results

Methods outline

To predict the stable crystal structure formed by the assembled atoms with a given chemical composition X , we used a machine-learning workflow summarized in Figure 1. This method involves two key technical components: a high-performance surrogate model for DFT formation energies and two different generative models for candidate crystal structures.

For the energy calculation, a CGCNN with the same architecture as in the original paper²⁸ was first pretrained from scratch on a set of 126,210 crystals for which DFT formation energies are available in the Materials Project. We refer to this model as the global model; it can accurately predict the baseline formation energies of diverse crystal structures but lacks the ability to discriminate the local energy difference of different atomic conformations for a given target system. Therefore, the pretrained global model was transformed into a model localized to the target system X . To this end, 1,000 virtual crystal structures were randomly generated, and their formation energies were calculated by performing single-point DFT calculations. The training structures were generated using either the Wyckoff position generator or random element substitution of existing crystals, as described below. Using this dataset, we performed transfer learning to adapt the pretrained global model to a local model applicable to the energy evaluation of different configurations for X . Here, the output layer was trained from scratch, whereas the pretrained weight parameters in the other layers were retained and fine-tuned (see the Methods section).

We developed and tested two algorithms for the generation of virtual crystals.

Method 1: Element substitution Element substitution of already synthesized or theoretically possible crystals with the same compositions as X is randomly performed.

Method 2: Wyckoff position generator For a target composition with the space group given a priori or predicted, the generator creates symmetry-restricted atomic coordinates randomly from all possible combinations of Wyckoff positions.

The element-substitution method cannot be applied unless a template is available for substitution, limiting the applicability of this method. Therefore, we developed the Wyckoff position generator for the generation of novel structural patterns. These two generators were used to generate training instances in the fine-tuning of CGCNN and the candidate structure in the high-throughput virtual screening. We used slightly different workflows for these two generators, as described below.

The generation of crystal structures by replacing the elements in the existing crystals mimics the process by which humans synthesize new crystalline materials in a laboratory. For a given query composition X , we collected a set of template crystal structures with the same compositional ratio as that of the X from the Materials Project database. A candidate structure was created by assigning the constituent elements of the query composition to the atomic coordinates of the selected template. Elements with the same composition fraction in the template and in the query were substituted. When one or more elements have the same composition fraction, the assignment could not be uniquely determined. In this case, substitution was performed on the most similar element pair with the normalized Euclidean distance of the 58 element descriptors in the XenonPy library^{30,40–42} used as the similarity measure. The element-substituted crystal structure inherits the atomic coordinates of the template structure. As an additional refinement step, a slight random perturbation was incorporated into the generated atomic coordinates. Considering that multiple crystals in the database belong to the same prototype structure (for example, 8,005 compounds have the same composition ratio $A_1B_1C_2$), a cluster-based template selection procedure was introduced. The objective is to select highly relevant templates with query composition X while maintaining the diversity of the template structures. We applied DBSCAN^{43,44} to classify the templates into clusters in which the chemical compositions were converted into 290-dimensional compositional descriptors using XenonPy. Then, only the templates belonging to the same cluster as the query X were selected. In addition, to eliminate structurally redundant templates, we used pymatgen’s StructureMatcher module to construct a unique set of templates that did not contain identical prototype structures. For virtual library creation, 1,000 structures were generated from each of the K_{temp} selected templates by perturbing the atomic coordinates and lattice constants. For the training dataset in the fine-tuning, we used 10 structures generated randomly for each template using the same procedure.

The Wyckoff position generator produces random crystal structures for a given composition with a prescribed space group. For a given space group of X , the algorithm enumerates all possible combinations of Wyckoff letters assigned to

the constituent elements in X , and randomly selects one labeling pattern, with all patterns having the same probability of being selected. With Wyckoff site multiplicity and symmetry restricted, the atomic coordinates and lattice parameters were generated uniformly from specific intervals. Structures generated with two or more atoms within a certain distance were excluded a posteriori. Here, a space group predictor was used to estimate the space group of X . The objective is to predict and limit the space group of the stable crystalline state for a given composition X . For the training set, we compiled a list of chemical compositions and the space groups of 33,159 stable crystal structures from the Materials Project database. Using this model, the space group of the crystal system for X was narrowed to the top K_{SG} candidates. In this study, we set $K_{SG} = 10$. Based on this setting, 1,000 training instances ($100 \times K_{SG}$) and 15,000 candidate crystals ($1,500 \times K_{SG}$) were generated for the fine-tuning and virtual screening steps, respectively.

The transferred energy prediction model was then used to perform exhaustive virtual screening using each of the two generators separately. Finally, DFT calculations were performed to optimize the narrowed-down promising structures that exhibited the lowest predicted energies using the Vienna Ab initio Simulation Package (VASP)⁴⁵ version 6.1.2, combined with projector augmented wave (PAW) pseudopotentials⁴⁶ (see the Methods section for detailed procedures). The top K lowest-energy structures were subjected to structural relaxation with DFT. In this study, we set $K = 10 \times K_{SG}$ and $K = 5 \times K_{temp}$ for the Wyckoff position generation and for the element substitution generation, respectively. Generally, the top K candidates that reached the lowest energies consisted of significantly similar structures, many of which converged to the same crystal structure during the structural relaxation phase. To eliminate this redundancy, we considered structural similarity when selecting the top K candidate structures to maintain high structural diversity (the Methods section).

Benchmark sets

In this study, the performance of the proposed CSP algorithm was evaluated and compared to that of USPEX using two benchmark sets. The first benchmark set (Dataset I) consists of 40 stable crystals selected based on a literature survey, as listed in Table 1. Dataset I was selected based on two criteria: the diversity of space groups, constituent elements, number of atoms, and element species; and the diversity of applications such as battery and thermoelectric materials. Due to the presence of a certain bias in the selection of Dataset I, 50 additional stable crystals were randomly selected from the Materials Project (Table 2) (Dataset II). The crystal structure data (CIF files) for the selected structures are provided in the Supplementary Data. For Datasets I and II, the number of atoms in the unit cell of the selected crystals ranged from 2 to 104 and 2 to 288, with mean values of 23.14 and 32.68, respectively. 30% of the benchmark crystals had more than 30 atoms; due to the computational complexity and search performance, these structures were expected to be unsolvable by conventional heuristic searches based on first-principles calculations in the majority of cases.

Space group prediction

In the virtual screening with the Wyckoff position generator, to narrow down the huge space of possible crystalline states, we introduced a multiclass discriminator that predicts the space group Y_{SG} of a given chemical composition X among the 230 distinct groups. The compositional features of X were encoded into the 290-dimensional descriptor vector using XenonPy^{30,40-42} (see the Methods section). Fully connected neural network models were trained to learn the mapping from the vectorized compositions to the 230 space groups. To train and test the classifier, we used 33,159 instances of chemical compositions with the space groups of the stable crystalline states compiled from the Materials Project database, from which 90 benchmark crystal structures were removed. Of the total sample set, 80% of the instances were used for training and the remainder was used for testing. To statistically evaluate the prediction accuracy, training and testing were repeated 100 times independently. The details of the model construction, including hyperparameter adjustment, are described in the Supplementary Information.

Figure 2 shows the change in the recall rate from the top 1 to the top 40 predictions; that is, the change in the proportion of true labels included in the top K most probable predicted class labels ($K_{SG} = 1, \dots, 40$). The recall rates in the top 1, 10, and 40 predictions were 60.22(± 0.87)%, 85.35(± 0.54)%, and 94.02(± 0.43)% on average, respectively. This result indicates that by narrowing down to the top 10 predicted labels, we can identify the space groups for 85.35(± 0.54)% of the various crystalline systems. Using this model, we selected 230 space groups to be screened by generating symmetry-restricted crystal structures for each of the top 10 candidate space groups. The top 10 recall rates for different space groups were varied from 0.00(± 0.00)% to 99.22(± 0.31)% as shown in Figure S1. The variability of the recall rate was partially correlated with the number of training instances in each space group.

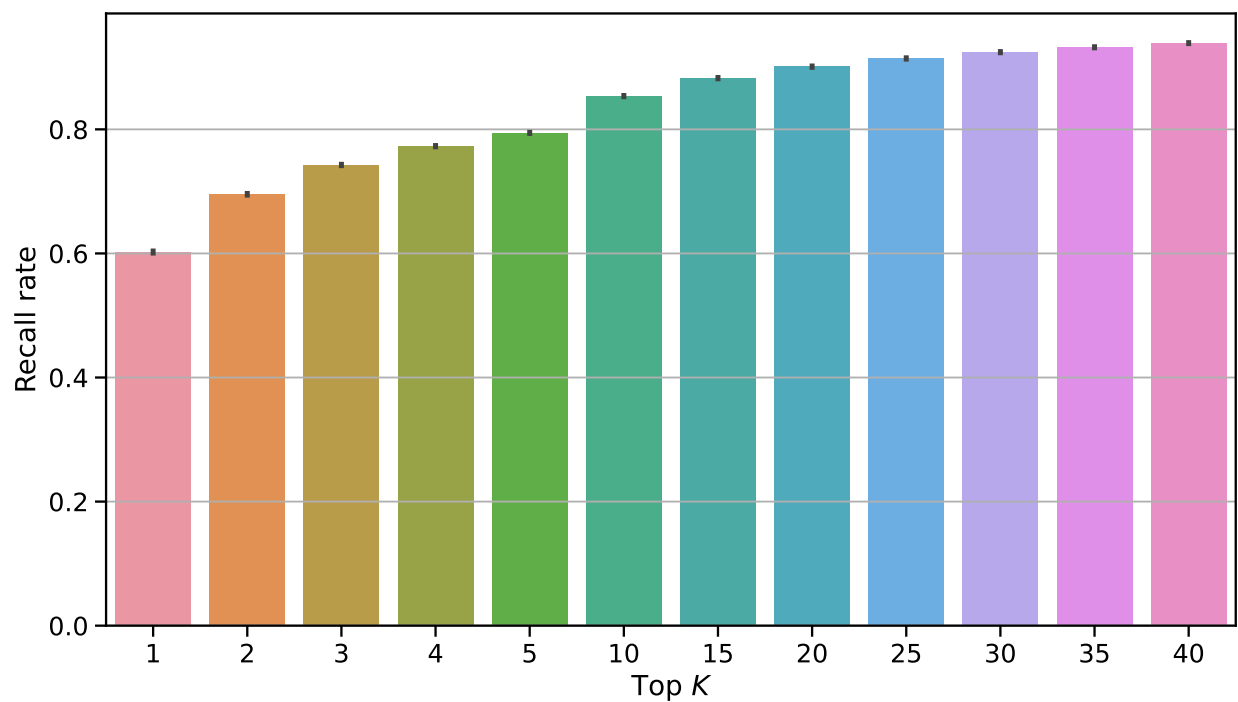


Figure 2. Change in the recall rate across the top 1 to the top 40 predictions of the space group. By narrowing down to the top 10 predicted labels, it is expected on average to enable the inclusion of the true space groups for 86.31% of the entire crystalline systems.

Energy prediction

For the global energy prediction model, the CGCNN was trained on 126,210 stable and unstable crystal structures, with their formation energies retrieved from the Materials Project; the 90 benchmark crystals were excluded from the training set. To validate the prediction capability and uncertainty of the global model, we randomly extracted 80% of the overall dataset and created 100 bootstrap sets. The mean absolute error (MAE) with respect to the 25,249 test cases reached 0.074 eV/atom on average, with a standard deviation of 0.003, which is comparable to that in previous studies, for example Xie & Grossman²⁸. Figure 3(a) shows the prediction results for the 90 benchmark crystals.

Note that the global model is inapplicable to the energy prediction of different conformations randomly generated for each X , as shown in Figure 3(c), and clearly failed to discriminate the energies of different conformations randomly generated for the 90 benchmark crystals. Here, we tested the prediction capability of the global model on the DFT energies of 100 randomly generated conformations for each of the 90 benchmark queries. It was found that the MAE decreased to 6.126 eV/atom on average with a standard deviation of 2.010.

To overcome this limited predictive ability, the pretrained global model was transferred to a model localized to the target system of X . For each X , the formation energies of 1,000 virtual crystals generated as described above were obtained by DFT single-point energy calculations, and the pretrained global model was fine-tuned to the target system. As shown in Figure 3(d), transfer learning successfully improved the prediction performance for the formation energies of the 9,000 additional conformations generated. The MAE reached 0.488 eV/atom on average with a standard deviation of 0.453, corresponding to a factor of 12.6 improvements compared to the MAE of the pretrained global energy prediction model.

CSP using the library generator based on element substitution

We used a fine-tuned surrogate energy predictor to sort the generated virtual crystals, narrowed them down to the top 5 structures for each template (as described above), and then performed structural relaxations using DFT. The J relaxed structures with the lowest DFT energies were used as the final set of predicted structures. Figure 4 shows the top 2 ($J = 2$) predictions and the true structures. Figure S2 shows the top 2 predicted structures for all of the 90 benchmark crystals. The top 5 prediction accuracies ($J = 5$) for Datasets I and II were 75.0% and 76.0%, respectively, and the top 10 accuracies ($J = 10$) for Datasets I and II were 82.5% and 86.0%, respectively. No significant differences are observed in the resulting accuracies between the two benchmark sets. Interestingly, no performance degradation was observed due to the increasing number of atoms in the unit cell. Of the 90 crystals, the five ($\text{NaCaAlPO}_5\text{F}_2$, $\text{K}_{20}\text{Ag}_8\text{As}_{12}\text{Se}_{36}$, $\text{Na}_1\text{W}_9\text{O}_{27}$, $\text{Na}_{80}\text{Fe}_{16}\text{P}_{32}\text{O}_{128}\text{F}_{32}$, and $\text{Y}_8\text{Si}_{10}\text{Ir}_{18}$) that could not be predicted had no template structures in the Materials Project with the same composition ratio. Excluding the five cases with no template, the top 10 accuracies for Datasets I and II reached 84.6% and 93.5%, respectively. These results suggest that crystal systems with template structures that have the same composition ratio can be largely predicted by substituting the elements in the existing crystals. For example, in the Materials Project, the proportion of crystals with one or more interchangeable template structures was 98.0%. A similar conclusion was reached in a previous study³³ that proposed a CSP algorithm based on elemental substitution using machine learning.

CSP using the Wyckoff position generator

For each predicted space group, the top 10 candidate structures with the lowest surrogate energies were selected for structural relaxation using DFT. Similar to the results of the template-based method, Figure 4 displays the top 2 predicted and true structures for some selected examples, and Figure S2 shows the top 2 predicted structures for the 90 benchmark crystals. For the top 10 predicted structures, 47.5% and 32.0% of the known stable structures were predicted for Datasets I and II, respectively. A significant decrease in performance was observed compared to the CSP algorithm using the template structure generator. One reason for this poor predictive power is the limited predictive performance of the space group. The top 10 predictions contained the true space groups of approximately 84.4% of the 90 benchmark crystals. This is almost the same level of accuracy as reported above.

Of the 76 crystals for which the space group was correctly identified, 19 and 24 true stable structures could not be predicted in Datasets I and II, respectively. Furthermore, of the 43 failure cases, 16 and 16 structures failed to generate true Wyckoff patterns, and 3 and 8 failed to obtain the ground truth, even though the true Wyckoff patterns were correctly generated in Datasets I and II, respectively. To elucidate the origin of these failures, we examined the generated structures in detail and found that most of the structures that failed to be predicted were low-symmetry structures with the space group number below 142, such as tetragonal, orthorhombic, and monoclinic structures. Because of their low

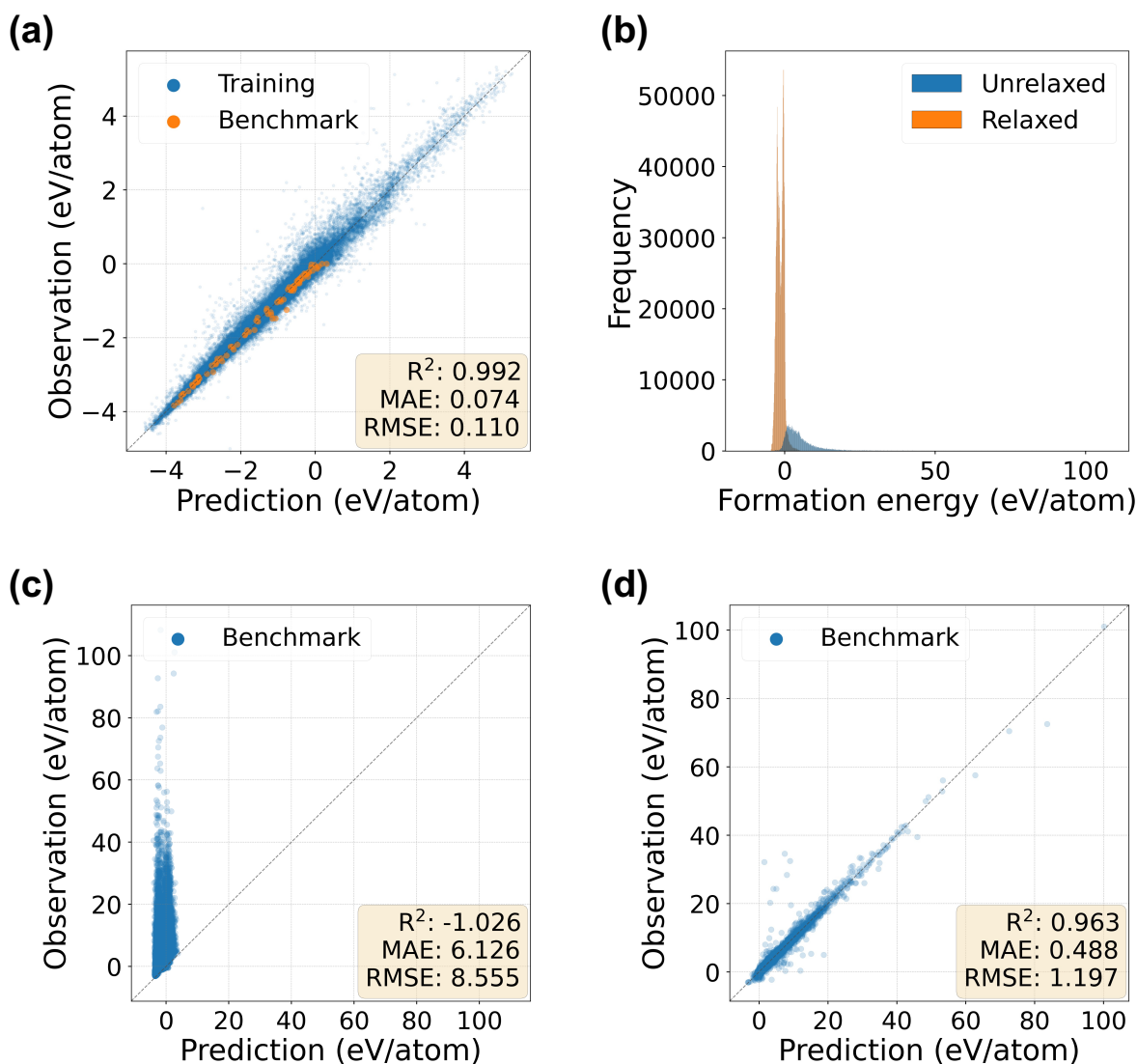


Figure 3. Performance of CGCNNs for the prediction of DFT formation energies with and without transfer learning. The root mean square error (RMSE), mean absolute error (MAE), and coefficient of determination (R^2) with respect to test instances are shown on each parity plot. (a) Results of the global model for the prediction of the relaxed formation energies of the 90 benchmark crystals (orange). (b) Histogram of the DFT formation energies of relaxed and randomly generated unrelaxed structures. (c)-(d) Prediction of unrelaxed formation energies of 100 randomly generated conformations for each of the 90 benchmark systems without and with fine-tuning of the pretrained global energy prediction model, respectively.

symmetry, structures belonging to these space groups have high degrees of freedom in their coordinate configurations. Furthermore, the number of combinations of Wyckoff patterns with the same multiplicity is greater for lower-symmetry space groups. For example, in space group 139, to which La_2CuO_4 and BaFe_2As_2 belong, there are two different Wyckoff letters with multiplicity 2, three different Wyckoff letters with multiplicity 4, and five different Wyckoff letters with multiplicity 8. Therefore, the number of possible Wyckoff pattern combinations is so large that the generated Wyckoff pattern candidates fail to contain true combinations.

As illustrated in Figure 4, many of the predicted structures that were determined to be failures were metastable structures that have been reported experimentally. For example, for TiO_2 ⁴⁷, the anatase type is the most stable structure according to first-principles calculations, whereas the predicted structure is the rutile type, which is known to be a metastable state. The true stable structure of Si_3N_4 ⁴⁸ is known to be a hexagonal structure, beta- Si_3N_4 , but the predicted structure is the willemite-II type, which was reported as a metastable structure by DFT calculations. In many cases, even the predicted crystal structures that were judged to be failures partially captured the structural features that are similar to the true structure. For example, the predicted structures of ZrO_2 , BN, Fe_3O_4 and SrTiO_3 did not precisely match the true structures but differed only slightly in atomic positions, as shown in Figure 4. The energy difference between the true and predicted structures of these compounds is < 5 meV/atom. Although stable structures are often not predicted with full accuracy for low-symmetry compounds, metastable structures or partial structural patterns can be predicted using our method.

Comparison with USPEX

As shown in Tables 1 and 2, USPEX with default settings and a ground truth space group succeeded in predicting only 32.5% and 10.0% of the benchmark crystals in Datasets I and II, respectively. The number of candidate structures in each generation of the genetic algorithm was set to 60, and the upper limit of the number of generations to be renewed was set to 100. For 10 crystals, USPEX failed to converge when the maximum number of iterations was 60.

USPEX is a computationally intensive method. We performed all of the calculations on the SQUID supercomputer system at Osaka University, which has two Intel Xeon Platinum 8368 CPUs with 76 cores running at 2.40 GHz at each node⁵⁰. Each crystal calculation was assigned to one node, and the number of MPI cores was set to 38 when the number of calculated atoms was less than 38, and was set to 76 otherwise. The median runtime per crystal was $66.0(\pm 102.6)$ hours. This is approximately 10 times slower than the CSP with a Wyckoff generator.

Discussion

This paper presents a machine-learning workflow for the efficient prediction of stable crystal structures with no iterative calculations. The essence of the proposed method is the shotgun-type virtual screening of crystal structures, in which a surrogate model that predicts DFT energy is simply used to screen a large number of virtual crystal structures, and the efficiently narrowed-down candidate structures are then relaxed by DFT calculations to predict the stable crystal structures. The technical components that play the key roles in this workflow are the surrogate model for energy prediction and the crystal structure generators. To train the surrogate model for DFT energy calculations, transfer learning of the pretrained CGCNN was performed to decrease the number of the training samples generated with DFT single-point calculations. To create virtual libraries of candidate crystal structures, a generator based on elemental substitutions in template crystals and a generator based on random combinations of Wyckoff positions were developed and tested. Of the 90 known crystal structures with a wide range of chemical compositions, symmetries, and structure types, the workflows using the generator based on element substitution and the Wyckoff position generator predicted 84.4% and 38.9% of the true structures, respectively. Thus, the proposed method significantly outperformed the prediction accuracy of USPEX which is the most widely used crystal structure prediction software that showed a prediction accuracy of less than 23.3%. Existing recursive algorithms that iterate over DFT calculations have not been thoroughly and comprehensively evaluated in terms of their prediction performance owing to their exceedingly high computational cost. To the best of our knowledge, our method is the simplest crystal structure prediction algorithm currently available. One of the contributions of this study is that this simple approach can efficiently solve for many crystal structures that cannot be predicted using conventional methods.

The comparison of the element-substitution-based generator and Wyckoff position generator showed that the prediction performance of the former was significantly better than that of the latter. Given a known template structure, the element-substitution-based generator was shown to be able to predict the stable structure with almost perfect

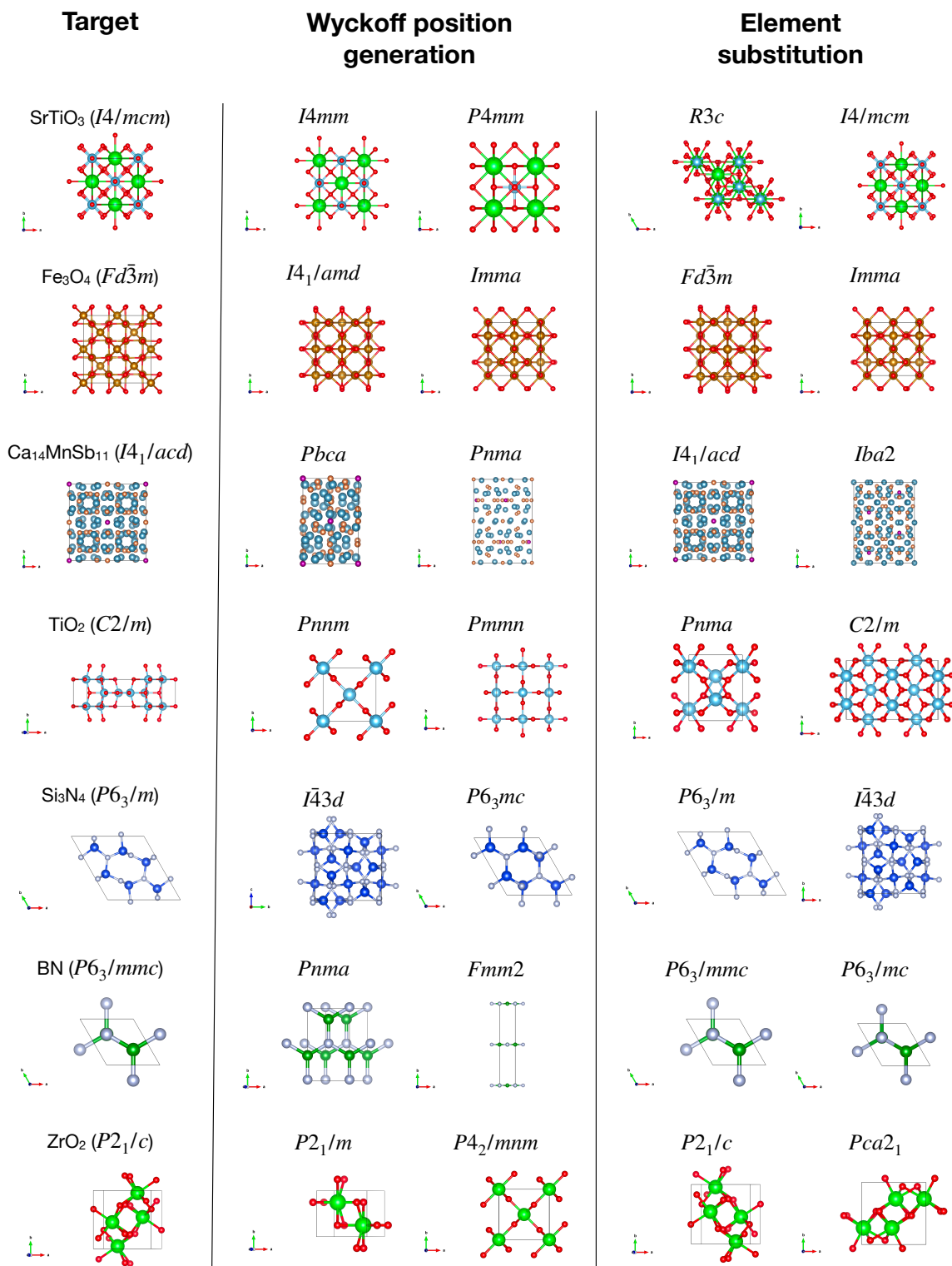


Figure 4. Examples of crystal structures predicted by the proposed CSP algorithm (depicted with VESTA⁴⁹ version 3.5.8). For each method (using the Wyckoff position generator or randomized element substitution), the predicted structures with the two lowest DFT energies are shown with the true stable structures.

accuracy, and approximately 98.0% of stable or metastable crystals in the Materials Project are known to have a counterpart that can act as a template structure. Therefore, it is estimated that many crystal systems can be predicted using element-substitution-based crystal-structure predictions. By contrast, while in principle virtual screening based on the Wyckoff position generator can predict new crystal structures, its prediction accuracy in benchmarking was not very high. The bottlenecks of this approach are the prediction accuracy of the space group and the limited ability of the Wyckoff position generator. With the current workflow, the upper bound of the accuracy of the top 20 space group predictors was approximately 87%. Even if the space group can be appropriately identified, the number of possible combinations of Wyckoff positions becomes too large for large systems with a large number of atoms, making it impossible to sample the true Wyckoff position using a generator following the brute-force approach for a completely random structure generation. Machine learning can help to resolve these bottlenecks.

Methods

Fine-tuning of CGCNN

To obtain a CGCNN localized to the energy prediction of a specific system with composition X , the pretrained global CGCNN model from Xie & Grossman²⁸ was fine-tuned using a sample set of 1,000 randomly generated conformations and their formation energies. The Wyckoff position generator was used to generate 100 training crystal structures from each of the top 10 candidate space groups given by the space group predictor. The pretrained model was copied to the target model, except for the output layer. Subsequently, a new output layer was added to the target model and its parameters were randomly initialized. We then trained the target model on the target dataset, hyperparameters learning rate and gradients clipping value were optimized by performing a grid search with range $\{0.01, 0.008, 0.006, 0.004, 0.002\}$, respectively, with early stopping of the MAE of the validation set. The number of epochs was fixed to 350.

DFT calculation details

All DFT calculations were performed using the Vienna Ab initio Simulation Package (VASP, version 6.1.2)⁵¹ with projector-augmented wave pseudopotentials⁴⁶. The exchange-correlation functional was considered using the Perdew–Burke–Ernzerhof formulation⁵² of the generalized gradient approximation. The Brillouin zone integration for the unit cells was automatically determined using the Γ -centered Monkhorst–Pack mesh function implemented in the VASP code. Single-point calculations (also called self-consistent field calculations) were performed on unrelaxed crystal structures that were virtually created to produce a training set for fine-tuning the pretrained CGCNN. The geometry of the final selected candidate structure was locally optimized by performing DFT calculations. To generate the inputs for VASP calculations, the “MPStaticSet” and “MPRelaxSet” presets implemented in Pymatgen⁵³ were used.

Structural similarity

To calculate the similarity between two structures i and j , we encoded the given structures into a vector-type structural descriptor with their local coordination information (site fingerprint) from all sites⁵⁴. Then, the structure similarity τ was calculated as the Euclidean distance between the crystal structure descriptors. Note that the criterion contains no elemental composition information and gets insensitivity for the low-symmetry structures. All the calculations were performed by Matminer⁵⁵, which is an open-source toolkit for materials data mining, with the same configuration as the Materials Project officially used. We visually inspected the difference between structures for different τ . In this study, structures with dissimilarity $\tau \leq 0.2$ were treated as the similar structures, and one will be randomly selected as the candidate.

USPEX calculation details

All USPEX calculations were performed using the official USPEX package (version 10.5)⁵⁶. We specified the calculation parameters “calculationMethod”, “calculationType”, and “optType” as “USPEX”, “300”, and “enthalpy”, respectively, to perform the crystal structure prediction task for bulk crystal using evolutionary algorithm (EA). The EA-related parameters were specified according to official suggestions⁵⁷. For example, the number of structures in each generation was set to $2 \times N$ rounded to the nearest 10, where N is the number of atoms. The calculation was terminated if the best structure did not change over 20 generations. Structural relaxation was executed automatically using the VASP (version

6.1.2) package combined with the projector-augmented wave pseudopotentials. The VASP calculation settings were the same as those described in the [DFT calculation details subsection](#).

Compositional descriptor

The chemical formula is $X = X_{c^1}^1 X_{c^2}^2 \dots X_{c^K}^K$ where X_k denotes a chemical element and c_k is its composition ratio. Each element of the descriptor vector of length 290 takes the following form:

$$\phi_{g,\eta}(X) = g(c^1, \dots, c^K, \eta(X^1), \dots, \eta(X^K)). \quad (1)$$

The scalar quantity $\eta(X^k)$ on the right-hand side represents a feature value of the element X^k such as the atomic weight, electronegativity, and polarizability. Using function g , the element features $\eta(X^1), \dots, \eta(X^K)$ with compositions c^1, \dots, c^K are converted into compositional features. For g , we use five different summary statistics: weighted mean, weighted variance, weighted sum, max-pooling, and min-pooling as given by

$$\begin{aligned} \phi_{\text{ave},\eta}(S) &= \frac{1}{\sum_{k=1}^K c^k} \sum_{k=1}^K c^k \eta(S^k), \\ \phi_{\text{var},\eta}(S) &= \frac{1}{\sum_{k=1}^K c^k} \sum_{k=1}^K c^k (\eta(S^k) - \phi_{\text{ave},\eta}(S))^2, \\ \phi_{\text{sum},\eta}(S) &= \sum_{k=1}^K c^k \eta(S^k), \\ \phi_{\text{max},\eta}(S) &= \max\{\eta(S^1), \dots, \eta(S^K)\}, \\ \phi_{\text{min},\eta}(S) &= \min\{\eta(S^1), \dots, \eta(S^K)\}. \end{aligned}$$

We used 58 distinct elemental features implemented in XenonPy. The full list of the 58 features is given in Liu, et al.⁴¹, including the atomic number, covalent radius, van der Waals radius, electronegativity, thermal conductivity, band gap, polarizability, boiling point, and melting point. In summary, composition X is characterized by a 290-dimensional descriptor vector ($= 58 \times 5$).

Table 1. Performance of the CSP algorithm with element substitution and Wyckoff position random crystal structure generators for the 40 crystals comprising Dataset I. The top 10 virtual structures with the lowest DFT energies from the two generators were proposed as the final candidate, respectively. USPEX, which was configured with default settings and a ground truth space group, was used as the baseline method. Results in columns R1 and R2 used the same hyperparameters except that the space group in R2 is strict to the ground truth. The \checkmark and \times symbols indicate success and failure, respectively. In the Wyckoff position generation column, the symbols in parentheses indicate whether the true Wyckoff pattern was successfully generated. In the element substitution column, the symbols in parentheses indicate whether a similar template structure ($\tau \leq 0.2$) was found. $-$ denotes a failed space group prediction, no template matched, and an unfinished searching task, respectively.

Composition	Number of atoms	Space group	Wyckoff position generation	Element substitution	USPEX	
					R1	R2
C	4	$R\bar{3}m$	\checkmark (\checkmark)	\checkmark (\checkmark)	\times	\times
Si	2	$Fd\bar{3}m$	\checkmark (\checkmark)	\checkmark (\checkmark)	\checkmark	\checkmark
GaAs	2	$F\bar{4}3m$	\checkmark (\checkmark)	\checkmark (\checkmark)	\checkmark	\checkmark
ZnO	4	$P6_3mc$	\checkmark (\checkmark)	\checkmark (\checkmark)	\checkmark	\checkmark
BN	4	$P6_3/mmc$	\times (\times)	\checkmark (\checkmark)	\times	\times
LiCoO ₂	16	$R\bar{3}m$	\checkmark (\checkmark)	\checkmark (\checkmark)	\times	\times
Bi ₂ Te ₃	5	$R\bar{3}m$	\checkmark (\checkmark)	\checkmark (\checkmark)	\times	\times
Ba(FeAs) ₂	5	$I4/mmm$	\checkmark (\checkmark)	\checkmark (\checkmark)	\times	\checkmark

Table 1 continued

Composition	Number of atoms	Space group	Wyckoff position generation	Element substitution	USPEX	
					R1	R2
SiO ₂	6	$I\bar{4}2d$	× (−)	× (✓)	×	×
VO ₂	6	$P4_2/mnm$	✓ (×)	✓ (✓)	×	✓
La ₂ CuO ₄	7	$I4/mmm$	× (×)	✓ (✓)	×	×
LiPF ₆	8	$R\bar{3}$	✓ (✓)	✓ (✓)	×	✓
Al ₂ O ₃	10	$R\bar{3}c$	✓ (✓)	✓ (✓)	✓	✓
SrTiO ₃	10	$I4/mcm$	× (×)	✓ (✓)	×	×
CaCO ₃	10	$R\bar{3}c$	✓ (✓)	✓ (✓)	×	✓
TiO ₂	12	$C2/m$	× (×)	× (✓)	×	✓
ZrO ₂	12	$P2_1/c$	× (×)	✓ (✓)	×	×
ZrTe ₅	12	$Cmcm$	× (×)	✓ (✓)	×	×
V ₂ O ₅	14	$Pmnn$	× (×)	× (×)	×	×
Si ₃ N ₄	14	$P6_3/m$	× (×)	✓ (✓)	✓	✓
Fe ₃ O ₄	14	$Fd\bar{3}m$	× (✓)	✓ (✓)	×	×
Mn(FeO ₂) ₂	14	$Fd\bar{3}m$	✓ (✓)	✓ (✓)	×	✓
ZnSb	16	$Pbca$	✓ (−)	✓ (✓)	×	✓
CoSb ₃	16	$Im\bar{3}$	✓ (✓)	✓ (✓)	×	×
LiBF ₄	18	$P3_121$	× (✓)	✓ (✓)	×	✓
Y ₂ Co ₁₇	19	$R\bar{3}m$	✓ (✓)	✓ (✓)	×	×
GeH ₄	20	$P2_12_12_1$	× (−)	✓ (✓)	−	×
CsPbI ₃	20	$Pnma$	× (×)	✓ (✓)	×	×
NaCaAlPO ₅ F ₂	24	$P2_1/m$	× (×)	−	×	×
LiFePO ₄	28	$Pnma$	✓ (✓)	✓ (✓)	×	×
Cu ₁₂ Sb ₄ S ₁₃	29	$I\bar{4}3m$	✓ (✓)	✓ (✓)	×	×
MgB ₇	32	$Imma$	× (×)	× (×)	−	×
Li ₃ PS ₄	32	$Pnma$	× (×)	× (×)	×	×
Cd ₃ As ₂	80	$I4_1/acd$	✓ (✓)	✓ (✓)	−	×
Li ₄ Ti ₅ O ₁₂	42	$C2/c$	× (×)	✓ (✓)	−	×
Ba ₂ CaSi ₄ (BO ₇) ₂	46	$I\bar{4}2m$	× (×)	× (×)	−	×
Ag ₈ GeS ₆	60	$Pna2_1$	× (✓)	✓ (✓)	−	×
Nd ₂ Fe ₁₄ B	68	$P4_2/mnm$	× (×)	✓ (✓)	−	−
Y ₃ Al ₅ O ₁₂	80	$Ia\bar{3}d$	✓ (✓)	✓ (✓)	−	×
Ca ₁₄ MnSb ₁₁	104	$I4_1/acd$	× (×)	✓ (✓)	−	−
Overall			19/40 = 47.5%	33/40 = 82.5%	5/40 = 12.5%	13/40 = 32.5%

Table 2. Performance of the CSP algorithm with element substitution and Wyckoff position random crystal structure generators for 50 randomly selected crystals from the Materials Project that comprise Dataset II. The top 10 virtual structures with the lowest DFT energies from the two generators were proposed as the final candidate, respectively. USPEX, which was configured with default settings and a ground truth space group, was used as the baseline method. The \checkmark and \times symbols indicate success and failure, respectively. In the Wyckoff position generation column, the symbols in parentheses indicate whether the true Wyckoff pattern was successfully generated. In the element substitution column, the symbols in parentheses indicate whether a similar template structure ($\tau \leq 0.2$) was found. $-$ denotes a failed space group prediction, no template matched, and an unfinished searching task, respectively.

Composition	Number of atoms	Space group	Wyckoff position generation	Element substitution	USPEX
CsCl	2	$Fm\bar{3}m$	\checkmark (\checkmark)	\checkmark (\checkmark)	$-$
MnAl	2	$P4/mmm$	\checkmark (\checkmark)	\checkmark (\checkmark)	$-$
HoHSe	3	$P\bar{6}m2$	\checkmark (\checkmark)	\checkmark (\checkmark)	\checkmark
ErCdRh ₂	4	$Fm\bar{3}m$	\checkmark (\checkmark)	\checkmark (\checkmark)	\times
Eu ₂ MgTl	4	$Fm\bar{3}m$	\checkmark (\checkmark)	\checkmark (\checkmark)	\times
Pm ₂ NiIr	4	$Fm\bar{3}m$	\checkmark (\checkmark)	\checkmark (\checkmark)	\times
VPt ₃	4	$I4/mmm$	\checkmark (\checkmark)	\checkmark (\checkmark)	\checkmark
Gd(SiOs) ₂	5	$I4/mmm$	\checkmark (\checkmark)	\checkmark (\checkmark)	\checkmark
LaAl ₃ Au	5	$I4mm$	\checkmark (\checkmark)	\checkmark (\checkmark)	\times
U ₂ SbN ₂	5	$I4/mmm$	\times (\checkmark)	\checkmark (\checkmark)	\times
MnGa(CuSe ₂) ₂	8	$I\bar{4}$	\times ($-$)	\checkmark (\checkmark)	\times
SmZnPd	9	$P\bar{6}2m$	\checkmark (\checkmark)	\checkmark (\checkmark)	\times
Sn(TePd ₃) ₂	9	$I4mm$	\times ($-$)	\checkmark (\checkmark)	\times
V ₅ S ₄	9	$I4/m$	\times (\checkmark)	\checkmark (\checkmark)	\times
Cs ₃ InF ₆	10	$Fm\bar{3}m$	\checkmark (\checkmark)	\checkmark (\checkmark)	\times
Eu(CuSb) ₂	10	$P4/nmm$	\times (\checkmark)	\checkmark (\checkmark)	\times
Rb ₂ TlAgCl ₆	10	$Fm\bar{3}m$	\checkmark (\checkmark)	\checkmark (\checkmark)	\times
Ca ₃ Ni ₇ B ₂	12	$R\bar{3}m$	\times (\checkmark)	\checkmark (\checkmark)	\times
DyPO ₄	12	$I4_1/amd$	\checkmark (\checkmark)	\checkmark (\checkmark)	\checkmark
LaSiIr	12	$P2_13$	\times (\checkmark)	\checkmark (\checkmark)	\times
SmVO ₄	12	$I4_1/amd$	\checkmark (\checkmark)	\checkmark (\checkmark)	\times
VCl ₅	12	$P\bar{1}$	\times (\checkmark)	\checkmark (\checkmark)	\times
YbP ₅	12	$P2_1/m$	$-$ ($-$)	\checkmark (\checkmark)	\times
Eu(Al ₂ Cu) ₄	13	$I4/mmm$	$-$ (\checkmark)	\checkmark (\checkmark)	$-$
Zr ₄ O	15	$R\bar{3}$	\times ($-$)	\times (\times)	\times
K ₂ Ni ₃ S ₄	18	$Fddd$	\times (\checkmark)	\checkmark (\checkmark)	\times
Sr(ClO ₃) ₂	18	$Fdd2$	\times (\checkmark)	\checkmark (\checkmark)	\times
LiSm ₂ IrO ₆	20	$P2_1/c$	\times (\checkmark)	\checkmark (\checkmark)	\times
Pr ₂ ZnPtO ₆	20	$P2_1/c$	\times (\checkmark)	\checkmark (\checkmark)	\times
Sc ₂ Mn ₁₂ P ₇	21	$P\bar{6}$	$-$ (\times)	\checkmark (\checkmark)	\times
LaSi ₂ Ni ₉	24	$I4_1/amd$	\checkmark (\checkmark)	\checkmark (\checkmark)	\times
CeCu ₅ Sn	28	$Pnma$	\checkmark (\checkmark)	\checkmark (\checkmark)	$-$

Table 2 continued

Composition	Number of atoms	Space group	Wyckoff position generation	Element substitution	USPEX
LiP(HO ₂) ₂	32	<i>Pna2₁</i>	× (−)	✓ (×)	×
Mg ₃ Si ₂ H ₄ O ₉	36	<i>P6₃cm</i>	× (−)	× (×)	×
Y ₄ Si ₅ Ir ₉	36	<i>P6₃/mmc</i>	× (✓)	−	×
Na(WO ₃) ₉	37	<i>R$\bar{3}$</i>	− (−)	−	−
Sm ₆ Ni ₂₀ As ₁₃	39	<i>P$\bar{6}$</i>	− (✓)	✓ (✓)	−
BaCaGaF ₇	40	<i>P2₁/c</i>	× (✓)	✓ (✓)	×
Tm ₁₁ Sn ₁₀	42	<i>I4/mmm</i>	− (×)	✓ (✓)	−
AlH ₁₂ (ClO ₂) ₃	44	<i>R$\bar{3}c$</i>	× (−)	✓ (✓)	×
K ₂ ZrSi ₂ O ₇	48	<i>P2₁/c</i>	× (✓)	✓ (×)	×
Ba ₃ Ta ₂ NiO ₉	60	<i>P$\bar{3}m1$</i>	× (×)	× (×)	×
LiZr ₂ (PO ₄) ₃	72	<i>P2₁/c</i>	× (×)	✓ (✓)	−
K ₅ Ag ₂ (AsSe ₃) ₃	76	<i>Pnma</i>	× (×)	−	×
Be ₁₇ Ru ₃	80	<i>Im$\bar{3}$</i>	✓ (✓)	✓ (✓)	✓
Cu ₃ P ₈ (S ₂ Cl) ₃	80	<i>Pnma</i>	× (×)	✓ (✓)	×
Al ₂ CoO ₄	84	<i>P3m1</i>	× (−)	✓ (✓)	×
Li ₆ V ₃ P ₈ O ₂₉	92	<i>P1</i>	− (×)	✓ (×)	−
ReBi ₃ O ₈	96	<i>P2₁3</i>	× (×)	✓ (✓)	×
Na ₅ FeP ₂ (O ₄ F) ₂	288	<i>Pbca</i>	− (−)	−	−
Overall			16/50 = 32.0%	43/50 = 86.0%	5/50 = 10.0%

Data availability

The data that support the findings of this study are available from the corresponding authors upon reasonable request.

Code availability

The codes of element substitution-based CSP are available from the GitHub website (https://github.com/yoshida-lab/XenonPy/blob/master/samples/CSP_with_element_substitution.ipynb).

Acknowledgements

This work was supported in part by a MEXT KAKENHI Grant-in-Aid for Scientific Research on Innovative Areas (Grant Number 19H05820), a JSPS Grant-in-Aid for Scientific Research (A) 19H01132 and a JSPS Grant-in-Aid for Early-Career Scientists 20K19866 from the Japan Society for the Promotion of Science (JSPS), and JST CREST Grant Number JPMJCR19I3.

Author Contributions

R.Y. and H.T. designed and conceived the project, and R.Y. wrote the preliminary draft of the paper. R.Y. and C.L. designed and developed the machine learning framework. C.L. developed the software and performed the experiments with the support of H.T., H.T., T.Y., K.W., and S.Y., who designed and tested the benchmark crystal structures. C.L., H.T., T.Y., and R.T. wrote and revised the manuscript. All authors discussed the results and commented on the manuscript.

Additional Information

Conflicts of Interest: The authors declare no competing interests.

References

1. Martoňák, R., Laio, A. & Parrinello, M. Predicting crystal structures: the parrinello-rahman method revisited. *Phys. Rev. Lett.* **90**, 075503 (2003).
2. Oganov, A. R. & Glass, C. W. Crystal structure prediction using *ab initio* evolutionary techniques: Principles and applications. *J. Chem. Phys.* **124**, 244704, DOI: [10.1063/1.2210932](https://doi.org/10.1063/1.2210932) (2006).
3. Pickard, C. J. & Needs, R. J. High-Pressure Phases of Silane. *Phys. Rev. Lett.* **97**, 045504, DOI: [10.1103/PhysRevLett.97.045504](https://doi.org/10.1103/PhysRevLett.97.045504) (2006).
4. Pickard, C. J. & Needs, R. J. Structure of phase III of solid hydrogen. *Nat. Phys.* **3**, 473–476, DOI: [10.1038/nphys625](https://doi.org/10.1038/nphys625) (2007).
5. Pickard, C. J. & Needs, R. J. *Ab Initio* random structure searching. *J. Phys. Condens. Matter* **23**, 053201 (2011).
6. Kirkpatrick, S., Gelatt, C. D. & Vecchi, M. P. Optimization by Simulated Annealing. *Science* **220**, 671–680, DOI: [10.1126/science.220.4598.671](https://doi.org/10.1126/science.220.4598.671) (1983).
7. Pannetier, J., Bassas-Alsina, J., Rodriguez-Carvajal, J. & Caignaert, V. Prediction of crystal structures from crystal chemistry rules by simulated annealing. *Nature* **346**, 343–345, DOI: [10.1038/346343a0](https://doi.org/10.1038/346343a0) (1990).
8. Wang, F. & Landau, D. P. Efficient, Multiple-Range Random Walk Algorithm to Calculate the Density of States. *Phys. Rev. Lett.* **86**, 2050–2053, DOI: [10.1103/PhysRevLett.86.2050](https://doi.org/10.1103/PhysRevLett.86.2050) (2001).
9. Wang, Y., Lv, J., Zhu, L. & Ma, Y. Crystal structure prediction via particle-swarm optimization. *Phys. Rev. B* **82**, 094116, DOI: [10.1103/PhysRevB.82.094116](https://doi.org/10.1103/PhysRevB.82.094116) (2010).
10. Zhang, Y., Wang, H., Wang, Y., Zhang, L. & Ma, Y. Computer-Assisted Inverse Design of Inorganic Electrides. *Phys. Rev. X* **7**, 011017, DOI: [10.1103/PhysRevX.7.011017](https://doi.org/10.1103/PhysRevX.7.011017) (2017).
11. Oganov, A. R., Lyakhov, A. O. & Valle, M. How Evolutionary Crystal Structure Prediction Works—and Why. *Acc. Chem. Res.* **44**, 227–237, DOI: [10.1021/ar1001318](https://doi.org/10.1021/ar1001318) (2011).
12. Lyakhov, A. O., Oganov, A. R., Stokes, H. T. & Zhu, Q. New developments in evolutionary structure prediction algorithm USPEX. *Comput. Phys. Commun.* **184**, 1172–1182, DOI: [10.1016/j.cpc.2012.12.009](https://doi.org/10.1016/j.cpc.2012.12.009) (2013).
13. Yamashita, T. *et al.* Crystal structure prediction accelerated by Bayesian optimization. *Phys. Rev. Mater.* **2**, 013803, DOI: [10.1103/PhysRevMaterials.2.013803](https://doi.org/10.1103/PhysRevMaterials.2.013803) (2018).
14. Terayama, K., Yamashita, T., Oguchi, T. & Tsuda, K. Fine-grained optimization method for crystal structure prediction. *npj Comput. Mater.* **4**, 32, DOI: [10.1038/s41524-018-0090-y](https://doi.org/10.1038/s41524-018-0090-y) (2018).
15. Jacobsen, T. L., Jørgensen, M. S. & Hammer, B. On-the-Fly Machine Learning of Atomic Potential in Density Functional Theory Structure Optimization. *Phys. Rev. Lett.* **120**, 026102, DOI: [10.1103/PhysRevLett.120.026102](https://doi.org/10.1103/PhysRevLett.120.026102) (2018).
16. Podryabinkin, E. V., Tikhonov, E. V., Shapeev, A. V. & Oganov, A. R. Accelerating crystal structure prediction by machine-learning interatomic potentials with active learning. *Phys. Rev. B* **99**, 064114, DOI: [10.1103/PhysRevB.99.064114](https://doi.org/10.1103/PhysRevB.99.064114) (2019).
17. Wang, Y., Lv, J., Zhu, L. & Ma, Y. CALYPSO: A method for crystal structure prediction. *Comput. Phys. Commun.* **183**, 2063–2070, DOI: [10.1016/j.cpc.2012.05.008](https://doi.org/10.1016/j.cpc.2012.05.008) (2012).
18. Rasmussen, C. E. & Williams, C. K. I. *Gaussian Processes for Machine Learning*. Adaptive Computation and Machine Learning (MIT Press, Cambridge, Mass, 2006).
19. Mockus, J. *Bayesian Approach to Global Optimization: Theory and Applications*. Mathematics and Its Applications. Soviet Series (Kluwer Academic, Dordrecht ; Boston, 1989).
20. Jain, A. *et al.* Commentary: The Materials Project: A materials genome approach to accelerating materials innovation. *APL Mater.* **1**, 011002, DOI: [10.1063/1.4812323](https://doi.org/10.1063/1.4812323) (2013).
21. The Materials Project. <https://materialsproject.org>. Accessed: 2023-03-20.
22. Curtarolo, S. *et al.* AFLOW: An automatic framework for high-throughput materials discovery. *Comput. Mater. Sci.* **58**, 218–226, DOI: [10.1016/j.commatsci.2012.02.005](https://doi.org/10.1016/j.commatsci.2012.02.005) (2012).

23. AFLOW: Atomic - Flow for Materials Discovery. <http://www.aflowlib.org>. Accessed: 2023-03-20.
24. Kirklin, S. *et al.* The Open Quantum Materials Database (OQMD): Assessing the accuracy of DFT formation energies. *npj Comput. Mater.* **1**, 15010, DOI: [10.1038/npjcompumats.2015.10](https://doi.org/10.1038/npjcompumats.2015.10) (2015).
25. OQMD: The Open Quantum Materials Database. <http://oqmd.org>. Accessed: 2023-03-20.
26. Chen, C., Ye, W., Zuo, Y., Zheng, C. & Ong, S. P. Graph networks as a universal machine learning framework for molecules and crystals. *Chem. Mater.* **31**, 3564–3572 (2019).
27. Choudhary, K. & DeCost, B. Atomistic line graph neural network for improved materials property predictions. *npj Comput. Mater.* **7**, 1–8 (2021).
28. Xie, T. & Grossman, J. C. Crystal Graph Convolutional Neural Networks for an Accurate and Interpretable Prediction of Material Properties. *Phys. Rev. Lett.* **120**, 145301, DOI: [10.1103/PhysRevLett.120.145301](https://doi.org/10.1103/PhysRevLett.120.145301) (2018).
29. Weiss, K., Khoshgoftaar, T. M. & Wang, D. A survey of transfer learning. *J. Big Data* **3**, 9, DOI: [10.1186/s40537-016-0043-6](https://doi.org/10.1186/s40537-016-0043-6) (2016).
30. Yamada, H. *et al.* Predicting Materials Properties with Little Data Using Shotgun Transfer Learning. *ACS Cent. Sci.* **5**, 1717–1730, DOI: [10.1021/acscentsci.9b00804](https://doi.org/10.1021/acscentsci.9b00804) (2019).
31. Hautier, G., Fischer, C., Ehrlacher, V., Jain, A. & Ceder, G. Data Mined Ionic Substitutions for the Discovery of New Compounds. *Inorg. Chem.* **50**, 656–663, DOI: [10.1021/ic102031h](https://doi.org/10.1021/ic102031h) (2011).
32. Wang, H.-C., Botti, S. & Marques, M. A. L. Predicting stable crystalline compounds using chemical similarity. *npj Comput. Mater.* **7**, 12, DOI: [10.1038/s41524-020-00481-6](https://doi.org/10.1038/s41524-020-00481-6) (2021).
33. Kusaba, M., Liu, C. & Yoshida, R. Crystal structure prediction with machine learning-based element substitution. *Comput. Mater. Sci.* **211**, 111496 (2022).
34. Bushlanov, P. V., Blatov, V. A. & Oganov, A. R. Topology-based crystal structure generator. *Comput. Phys. Commun.* **236**, 1–7, DOI: [10.1016/j.cpc.2018.09.016](https://doi.org/10.1016/j.cpc.2018.09.016) (2019).
35. Fredericks, S., Parrish, K., Sayre, D. & Zhu, Q. PyXtal: A Python library for crystal structure generation and symmetry analysis. *Comput. Phys. Commun.* **261**, 107810, DOI: [10.1016/j.cpc.2020.107810](https://doi.org/10.1016/j.cpc.2020.107810) (2021).
36. Hu, J. *et al.* Contact map based crystal structure prediction using global optimization. *CrystEngComm* **23**, 1765–1776, DOI: [10.1039/d0ce01714k](https://doi.org/10.1039/d0ce01714k) (2021).
37. Kim, B., Lee, S. & Kim, J. Inverse design of porous materials using artificial neural networks. *Sci. Adv.* **6**, eaax9324, DOI: [10.1126/sciadv.aax9324](https://doi.org/10.1126/sciadv.aax9324) (2020).
38. Zhu, Q., Oganov, A. R., Glass, C. W. & Stokes, H. T. Constrained evolutionary algorithm for structure prediction of molecular crystals: Methodology and applications. *Acta Crystallogr. B: Struct. Sci.* **68**, 215–226, DOI: [10.1107/S0108768112017466](https://doi.org/10.1107/S0108768112017466) (2012).
39. Lee, I.-H. & Chang, K. Crystal structure prediction in a continuous representative space. *Comput. Phys. Commun.* **194**, 110436, DOI: [10.1016/j.compmatsci.2021.110436](https://doi.org/10.1016/j.compmatsci.2021.110436) (2021).
40. Wu, S., Lambard, G., Liu, C., Yamada, H. & Yoshida, R. iQSPR in XenonPy: A Bayesian Molecular Design Algorithm. *Mol. Inform.* **39**, 1900107, DOI: [10.1002/minf.201900107](https://doi.org/10.1002/minf.201900107) (2020).
41. Liu, C. *et al.* Machine Learning to Predict Quasicrystals from Chemical Compositions. *Adv. Mater.* **33**, 2102507, DOI: [10.1002/adma.202102507](https://doi.org/10.1002/adma.202102507) (2021).
42. Xenonpy platform. <https://github.com/yoshida-lab/XenonPy>. Accessed: 2023-03-20.
43. Ester, M., Kriegel, H.-P., Sander, J. & Xu, X. A density-based algorithm for discovering clusters in large spatial databases with noise. In *Proceedings of the Second International Conference on Knowledge Discovery and Data Mining*, KDD'96, 226–231 (AAAI Press, Portland, Oregon, 1996).
44. Schubert, E., Sander, J., Ester, M., Kriegel, H. P. & Xu, X. DBSCAN Revisited, Revisited: Why and How You Should (Still) Use DBSCAN. *ACM Trans. Database Syst.* **42**, 1–21, DOI: [10.1145/3068335](https://doi.org/10.1145/3068335) (2017).
45. Kresse, G. & Furthmüller, J. Efficient iterative schemes for *ab initio* total-energy calculations using a plane-wave basis set. *Phys. Rev. B* **54**, 11169–11186, DOI: [10.1103/PhysRevB.54.11169](https://doi.org/10.1103/PhysRevB.54.11169) (1996).

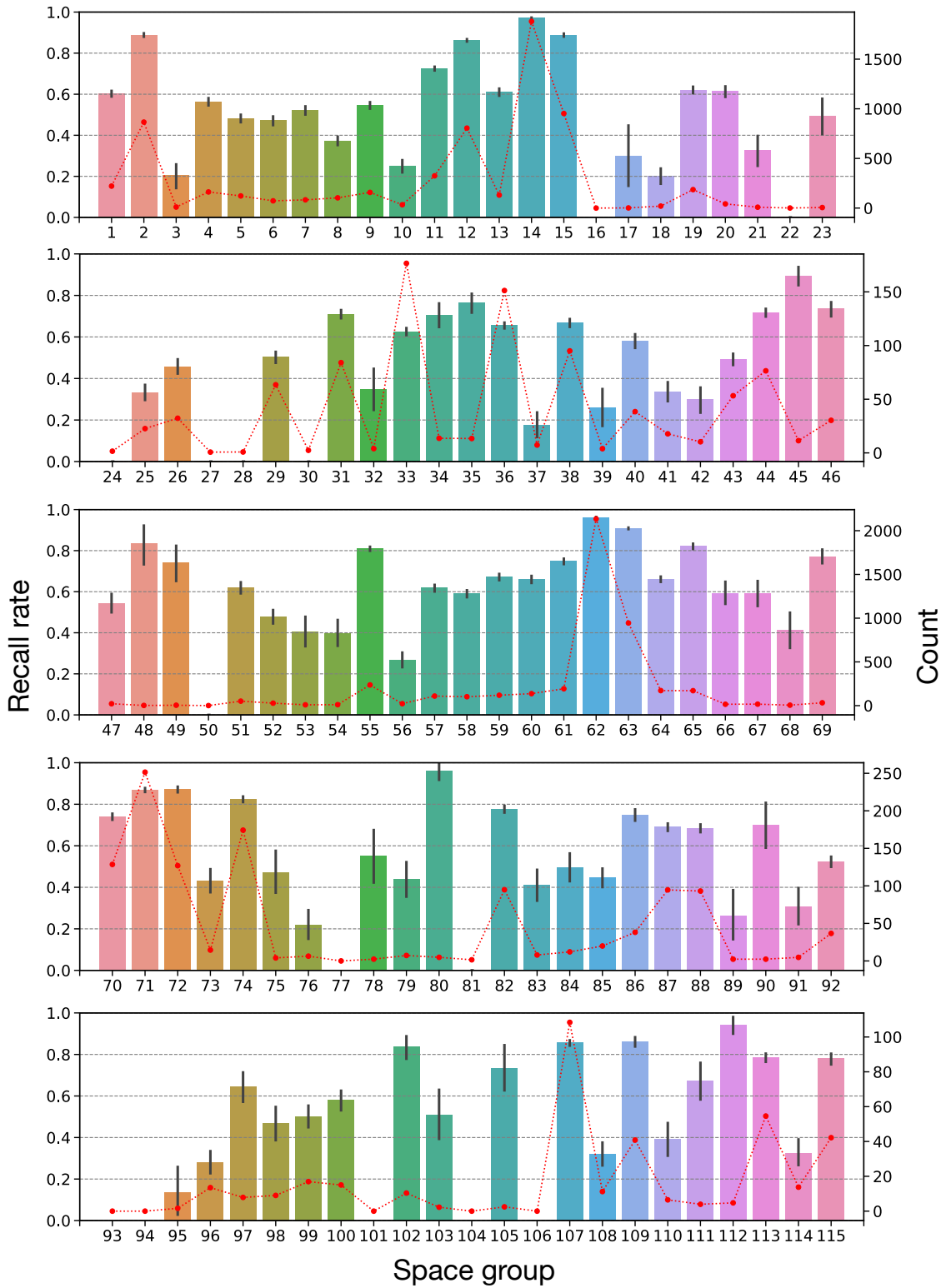
46. Blöchl, P. E. Projector augmented-wave method. *Phys. Rev. B* **50**, 17953–17979, DOI: [10.1103/PhysRevB.50.17953](https://doi.org/10.1103/PhysRevB.50.17953) (1994).
47. Cui, Z.-H., Wu, F. & Jiang, H. First-principles study of relative stability of rutile and anatase TiO₂ using the random phase approximation. *Phys. Chem. Chem. Phys.* **18**, 29914–29922, DOI: [10.1039/C6CP04973G](https://doi.org/10.1039/C6CP04973G) (2016).
48. Kroll, P. Pathways to metastable nitride structures. *J. Solid State Chem.* **176**, 530–537, DOI: [10.1016/S0022-4596\(03\)00300-1](https://doi.org/10.1016/S0022-4596(03)00300-1) (2003).
49. Momma, K. & Izumi, F. VESTA3 for three-dimensional visualization of crystal, volumetric and morphology data. *J. Appl. Cryst.* **44**, 1272–1276, DOI: [10.1107/S0021889811038970](https://doi.org/10.1107/S0021889811038970) (2011).
50. Squid (supercomputer for quest to unsolved interdisciplinary datascience). <http://www.hpc.cmc.osaka-u.ac.jp/en/squid/>. Accessed: 2023-03-20.
51. Kresse, G. & Furthmüller, J. Efficient iterative schemes for ab initio total-energy calculations using a plane-wave basis set. *Phys. Rev. B* **54**, 11169 (1996).
52. Perdew, J. P., Burke, K. & Ernzerhof, M. Generalized gradient approximation made simple. *Phys. Rev. Lett.* **77**, 3865 (1996).
53. Ong, S. P. *et al.* Python materials genomics (pymatgen): A robust, open-source python library for materials analysis. *Comput. Mater. Sci.* **68**, 314–319 (2013).
54. Zimmermann, N. E. R., Horton, M. K., Jain, A. & Haranczyk, M. Assessing local structure motifs using order parameters for motif recognition, Interstitial Identification, and diffusion path characterization. **4**, 34, DOI: [10.3389/fmats.2017.00034](https://doi.org/10.3389/fmats.2017.00034).
55. Ward, L. *et al.* Matminer: An open source toolkit for materials data mining. **152**, 60–69, DOI: [10.1016/j.commatsci.2018.05.018](https://doi.org/10.1016/j.commatsci.2018.05.018).
56. Uspex downloads. <https://uspex-team.org/en/uspex/downloads>. Accessed: 2023-03-20.
57. Uspex manual. https://uspex-team.org/online_utilities/tmp/uspex_manual_release/EnglishVersion/uspex_manual_english/index.html. Accessed: 2023-03-20.
58. Akiba, T., Sano, S., Yanase, T., Ohta, T. & Koyama, M. Optuna: A next-generation hyperparameter optimization framework. In *Proceedings of the 25th ACM SIGKDD international conference on knowledge discovery & data mining*, 2623–2631 (2019).

Space group predictor

Using 33,071 stable crystal structures obtained from the Materials Project database and their space groups, we constructed a fully connected neural network model that classifies any composition into one of the 212 space groups. All samples of the 90 benchmark crystal structures were removed from the dataset. The split ratios of the training and test sets were 80% and 20%, respectively. 5-fold cross-validation was looped with the training set to identify the hyperparameter pairs with the highest average prediction accuracy. Using the validation set, the hyperparameters of the models were selected by Bayesian optimization using the Optuna Python library (the number of trials was set to 200)⁵⁸ from the candidate set, the number of layers = {2, 3, 4}, the dropout ratio = {0, 0.1, 0.2}, and the number of neurons for each layer was set to $N \times \kappa$. Here, N denotes the number of neurons in the previous layer. $\kappa = 0.8 \sim 0.95$ is the hyperparameter. Finally, we calculate the predictive performance of the test set of the MLP model trained on the training set using the hyperparameters selected by optuna. Random data partitioning was repeated 100 times independently to examine the mean and variance of prediction accuracy. The top 10 precision, recall, and F_1 scores are 0.8535(± 0.0053), 0.8535(± 0.0054), and 0.8535(± 0.0054), respectively. Figure S1 shows the recall rate versus the number of training data points for each space group. The top 10 recall rate varied widely from 0.0000(± 0.0000) to 0.9922(± 0.0031) among the different space groups. The variability of the recall rate was partially correlated with the number of training instances in each space group.

Prediction of unit cell volumes

Using 33,071 stable crystal structures from the Materials Project database and their cell volumes, we constructed a fully connected neural network model for the prediction of the unit cell volume for any composition. All samples of the 90 benchmark crystal structures were removed from the dataset. The split ratios of the training and test sets were 80% and 20%, respectively. 5-fold cross-validation was performed with the training set to identify the hyperparameter pairs with the highest average prediction accuracy. Using the validation set, the hyperparameters of the models were selected by Bayesian optimization using the Optuna Python library (the number of trials was set to 200) from the candidate set, number of layers = {2, 3, 4}, dropout ratio = {0, 0.1, 0.2}, and the number of neurons in each layer was set to $N \times \kappa$. Here, N denotes the number of neurons in the previous layer. $\kappa = 0.8 \sim 0.95$ is the hyperparameter. Finally, we calculate the predictive performance of the test set of the MLP model trained on the training set using the hyperparameters selected by Optuna. The mean absolute error (MAE), root mean square error (RMSE), and R^2 of the predictions for the test set were 53.048 (± 3.177) eV, 90.362 (± 6.007) eV, and 0.973 (± 0.004) eV, respectively. Performance metrics were averaged over 100 bootstrap sets.



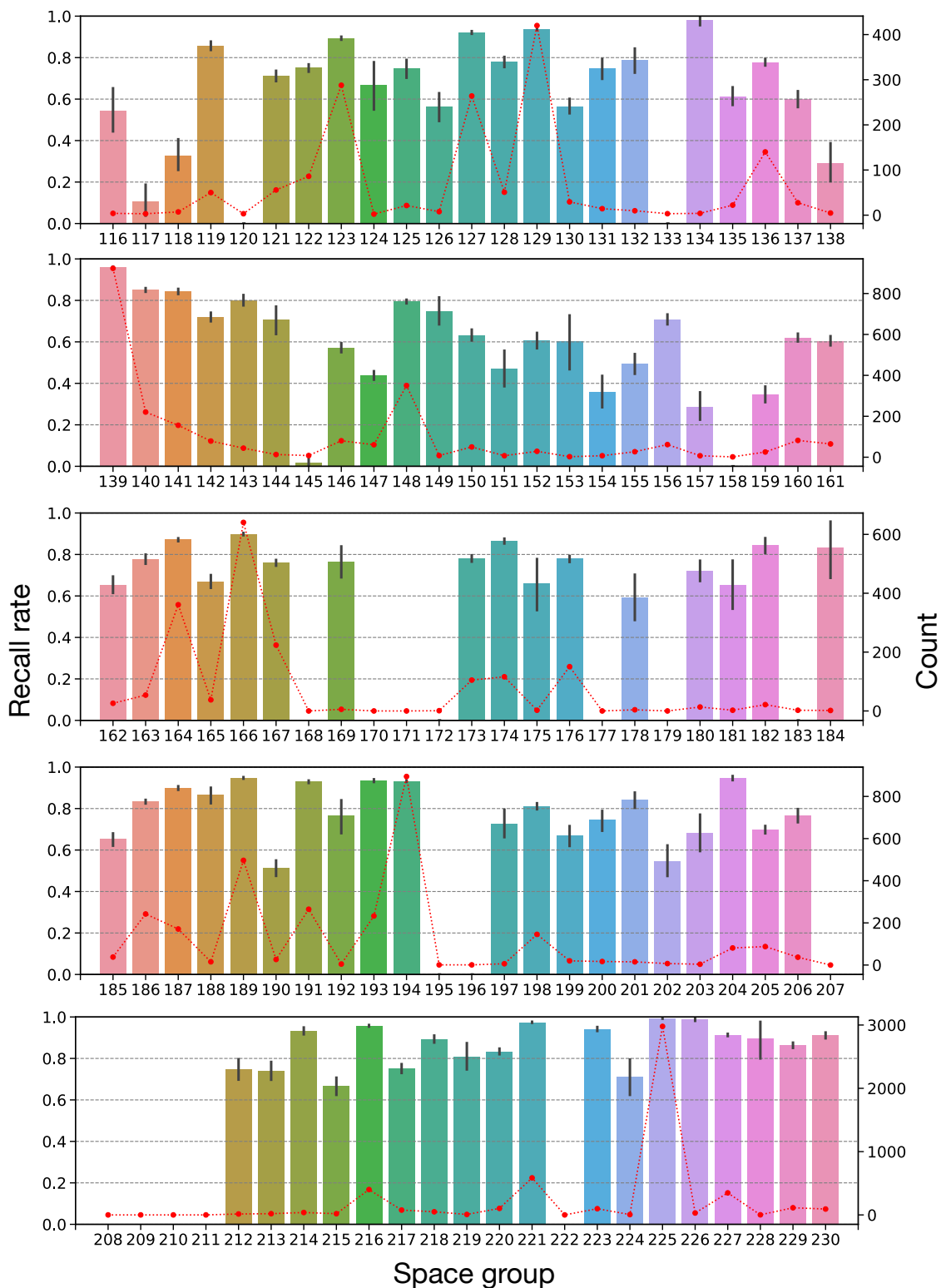
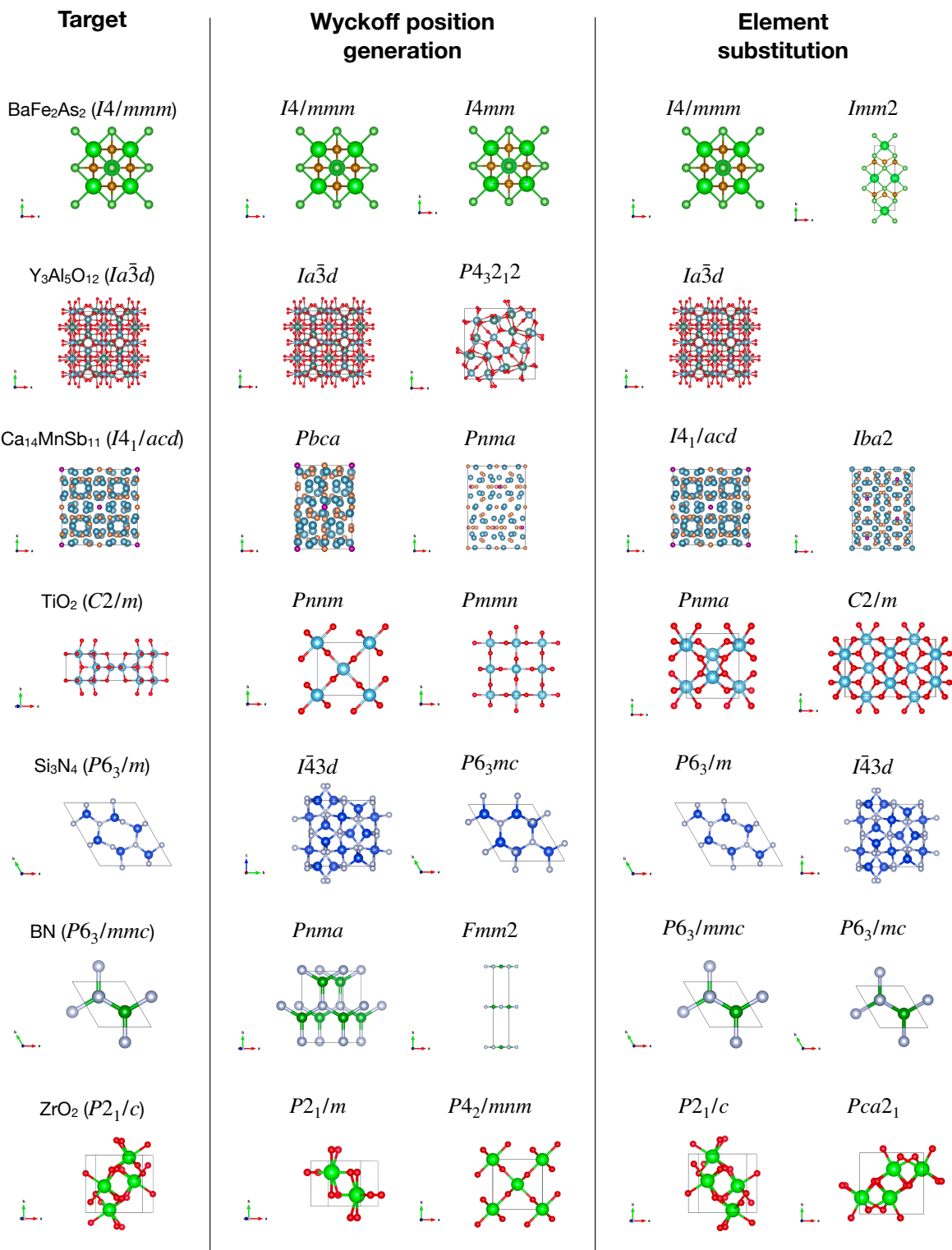
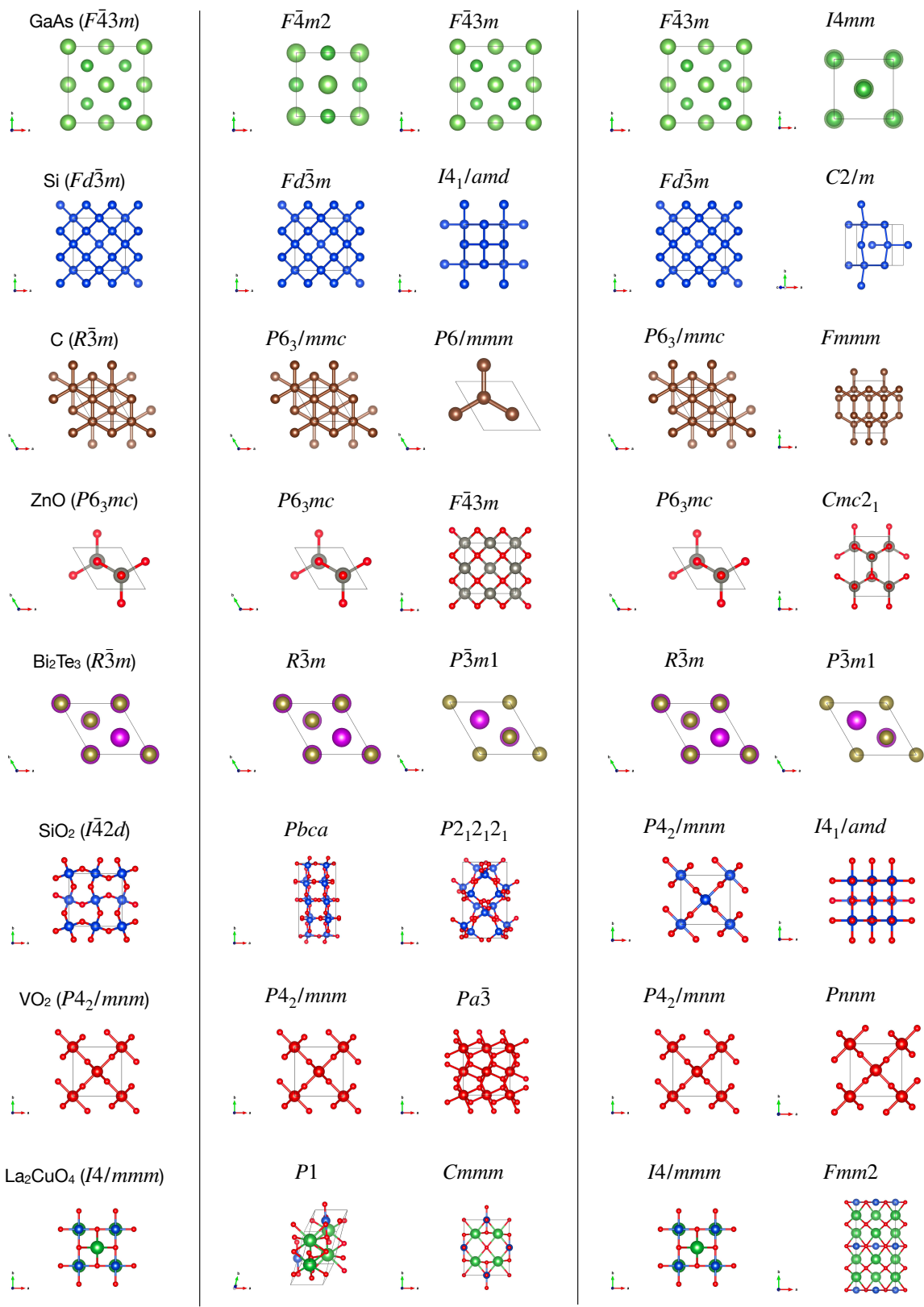
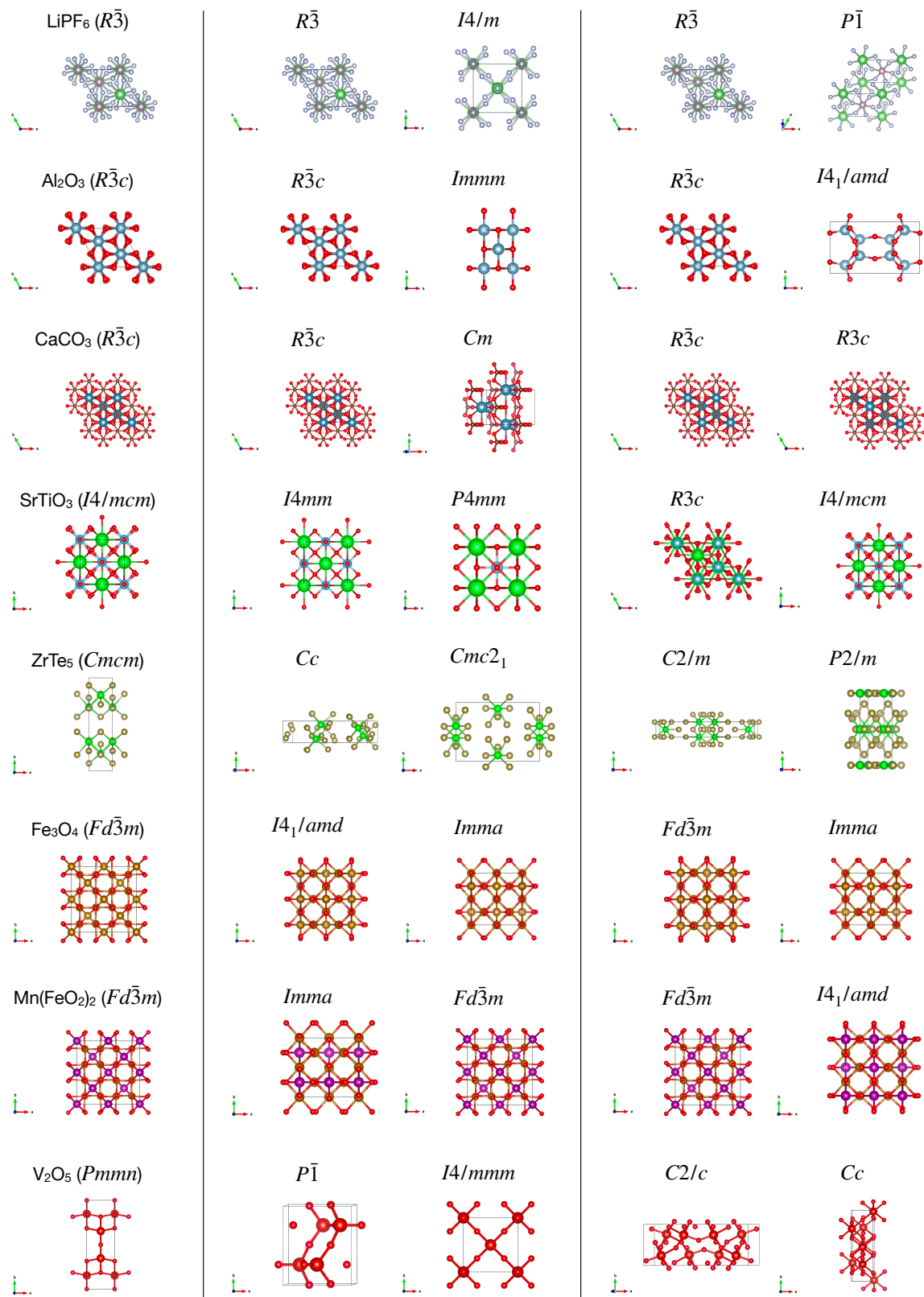


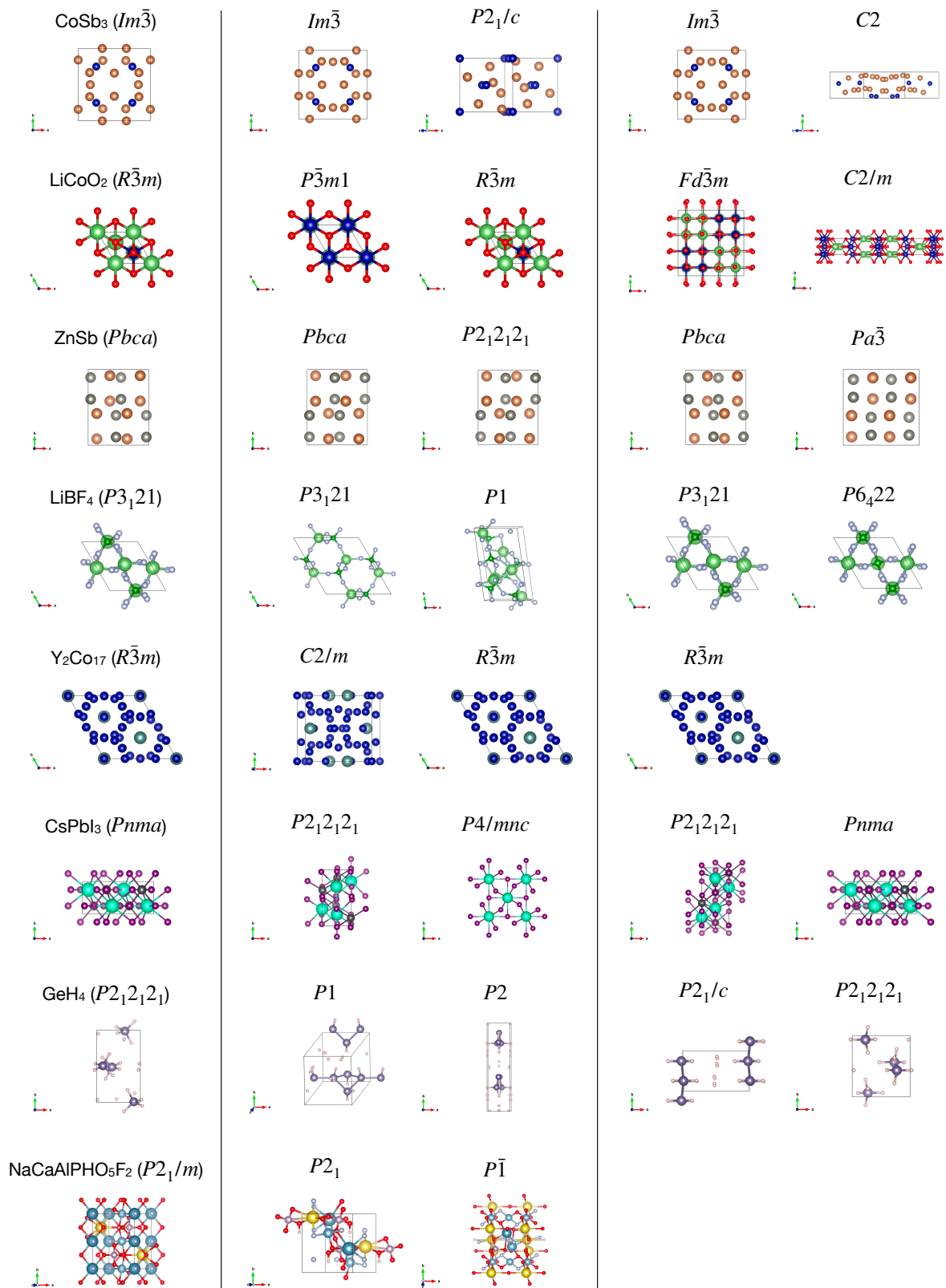
Figure S1. The recall rate of the top 10 predictions and the number of training instances for each space group. The training and testing were repeated 100 times independently. Color bars show the prediction recall rate with error bars representing the standard deviation for each space group. Red dashed line shows the average number of training instances.

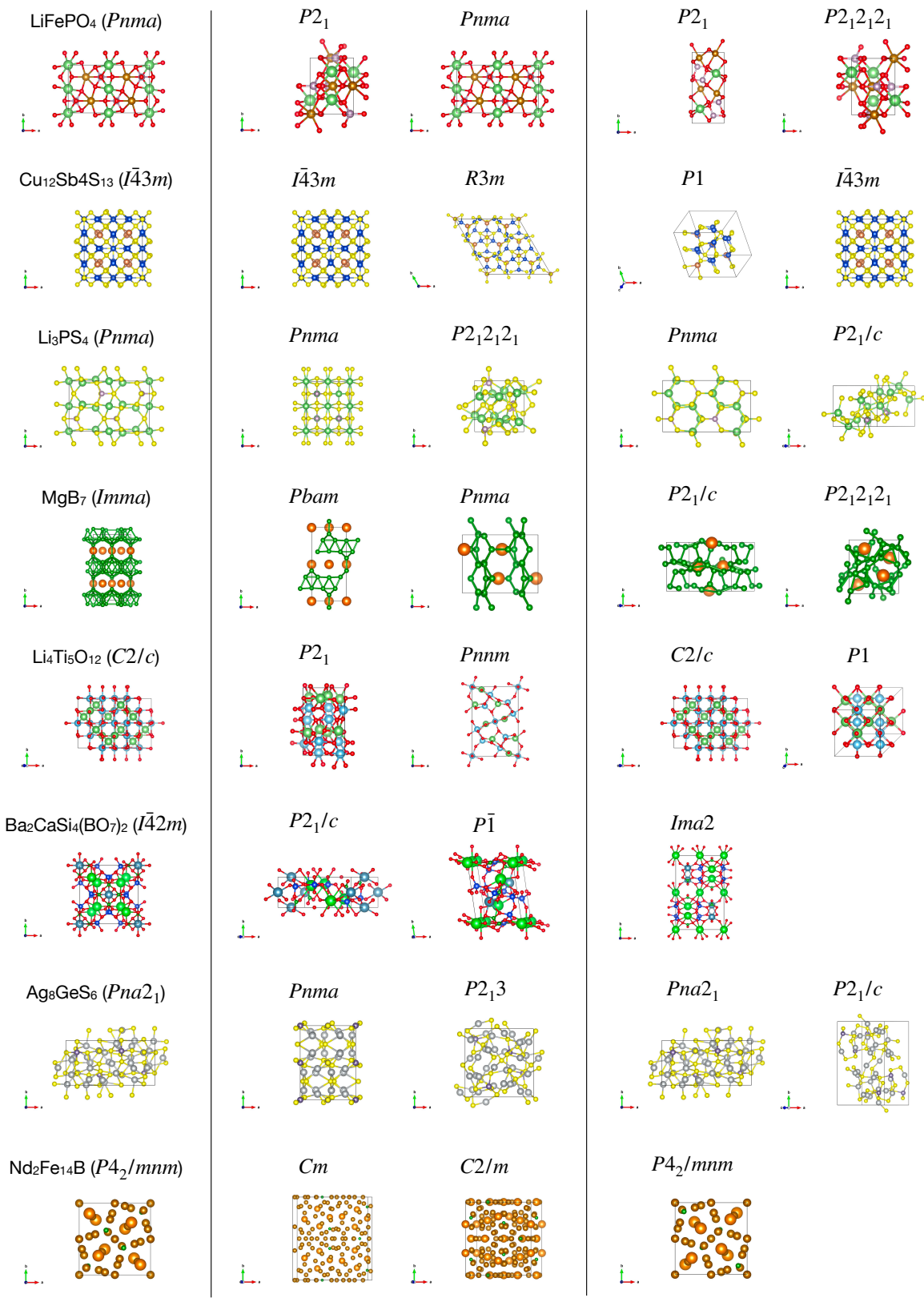
Visualization of solved structures



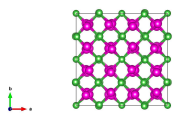




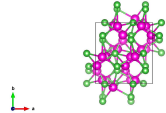




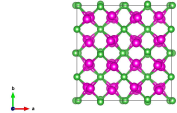
Cd_3As_2 ($I4_1/acd$)



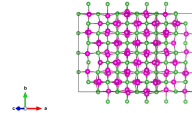
$Pbca$



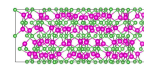
$Ia\bar{3}$



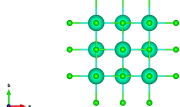
$C2/c$



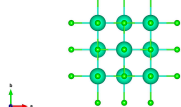
Cc



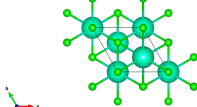
CsCl ($Fm\bar{3}m$)



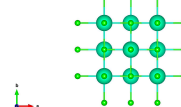
$Fm\bar{3}m$



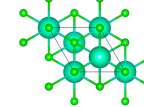
$R\bar{3}m$



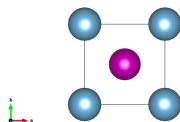
$Fm\bar{3}m$



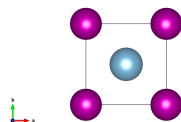
$R\bar{3}m$



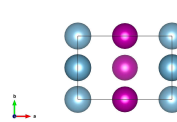
MnAl ($P4/mmm$)



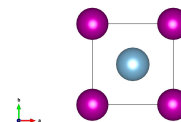
$P4/mmm$



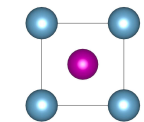
$Amm2$



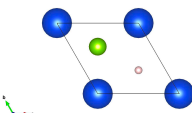
$P4/mmm$



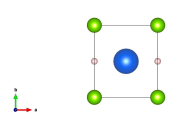
$Pm\bar{3}m$



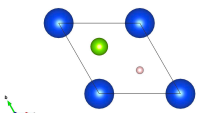
HoHSe ($P\bar{6}m2$)



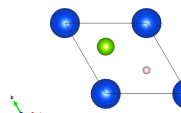
$Pmm2$



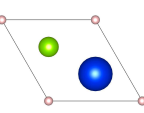
$P\bar{6}m2$



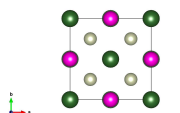
$P\bar{6}m2$



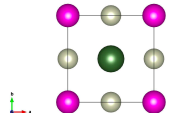
$P\bar{6}m2$



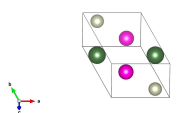
ErCdRh_2 ($Fm\bar{3}m$)



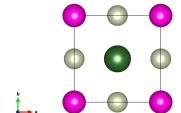
$P4/mmm$



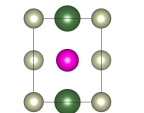
$P\bar{1}$



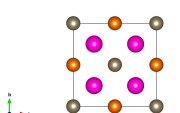
$P4/mmm$



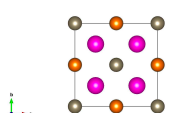
$Pmmm$



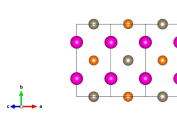
Eu_2MgTi ($Fm\bar{3}m$)



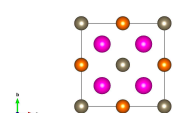
$Fm\bar{3}m$



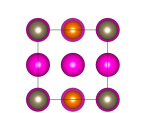
$C2/m$



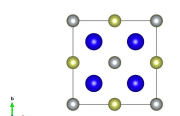
$Fm\bar{3}m$



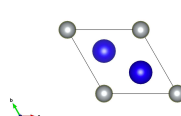
$I\bar{4}m2$



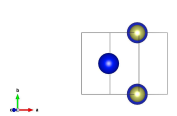
Pm_2NiIr ($Fm\bar{3}m$)



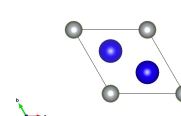
$P\bar{3}m1$



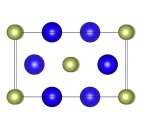
Pm



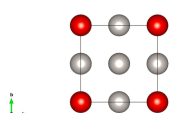
$P\bar{3}m1$



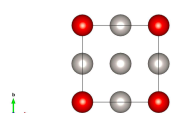
$C2/m$



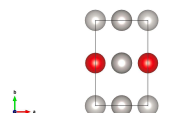
VPt_3 ($I4/mmm$)



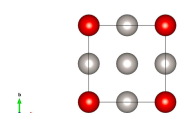
$I4/mmm$



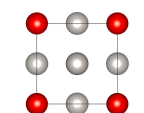
$Pmm2$



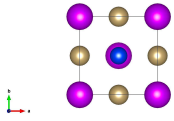
$I4/mmm$



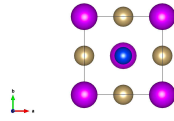
$Pm\bar{3}m$



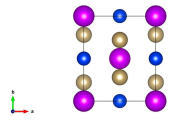
Gd(SiOs)₂ (*I4/mmm*)



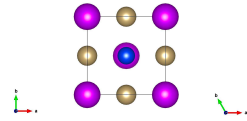
I4/mmm



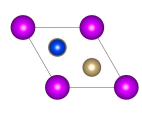
Immm



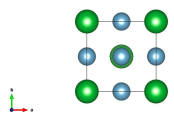
I4/mmm



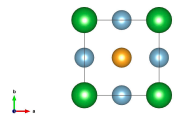
P3m1



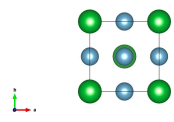
LaAl₃Au (*I4mm*)



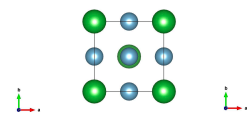
P4mm



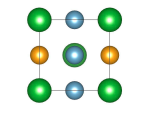
I4mm



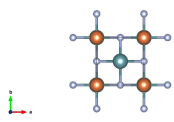
I4mm



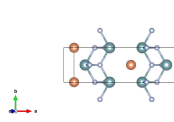
I4m2



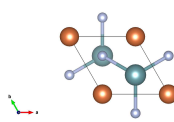
U₂Sb1N₂ (*I4/mmm*)



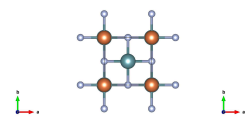
Cm



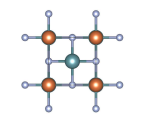
P3m1



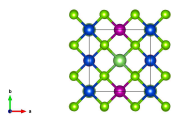
I4/mmm



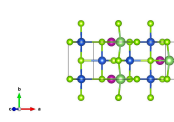
Immm



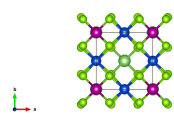
MnGa(CuSe₂)₂ (*I4*)



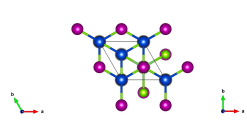
Cm



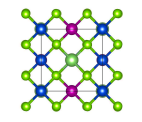
I42m



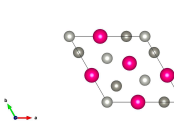
R3m



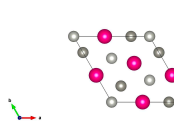
I4



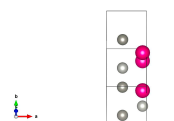
SmZnPd (*P62m*)



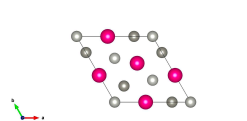
P62m



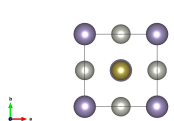
P1



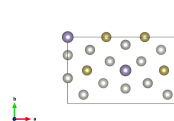
P62m



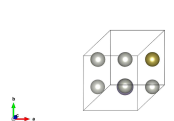
Sn(TePd₃)₂ (*I4mm*)



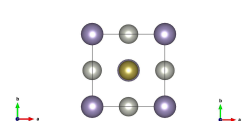
C2



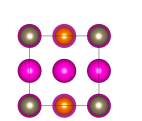
P1



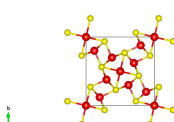
I4mm



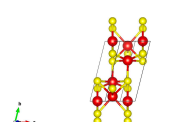
I4m2



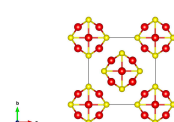
V₅S₄ (*I4/m*)



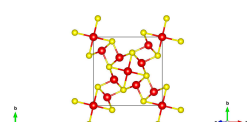
P1



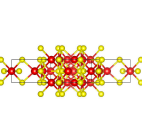
I4/mmm



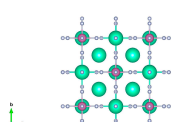
I4/m



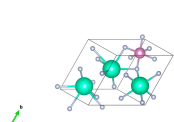
C2/m



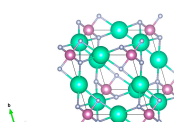
Cs₃InF₆ (*Fm3m*)



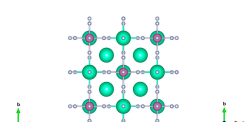
P1



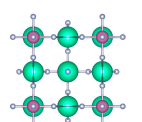
P1



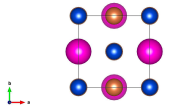
Fm3m



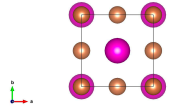
I4/mmm



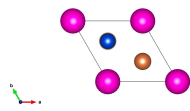
Eu(CuSb)₂ (*P4/nmm*)



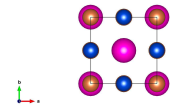
P4mm



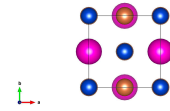
P6₃/mmc



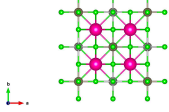
I4/mmm



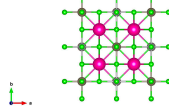
P4/nmm



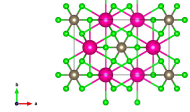
Rb₂TlAgCl₆ (*Fm $\bar{3}$ m*)



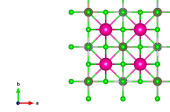
Fm $\bar{3}$ m



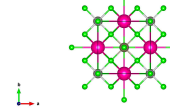
C2/m



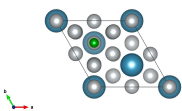
Fm $\bar{3}$ m



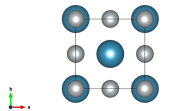
I4/mmm



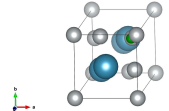
Ca₃Ni₇B₂ (*R $\bar{3}$ m*)



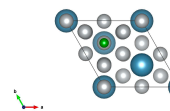
Immm



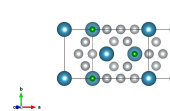
P $\bar{1}$



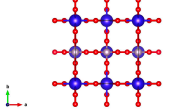
R $\bar{3}$ m



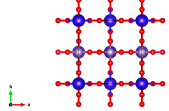
C2/m



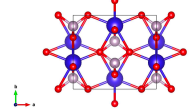
DyPO₄ (*I4₁/amd*)



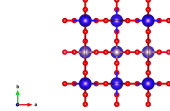
I4₁/amd



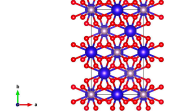
Cmcm



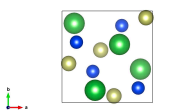
I4₁/amd



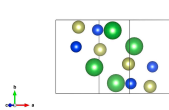
Fddd



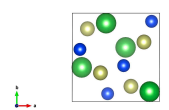
LaSi₄ (*P2₁3*)



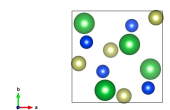
P2₁/c



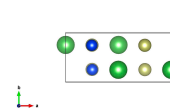
P1



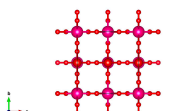
P2₁3



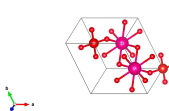
Pnma



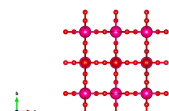
SmVO₄ (*I4₁/amd*)



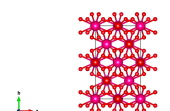
P1



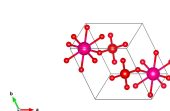
I4₁/amd



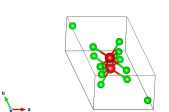
Fddd



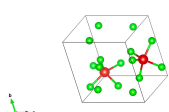
P1



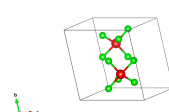
VCl₅ (*P $\bar{1}$*)



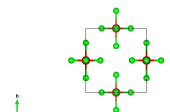
P1



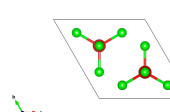
P1



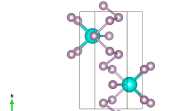
Pmnn



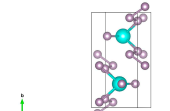
P6₃/mmc



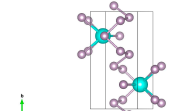
YbP₅ (*P2₁/m*)



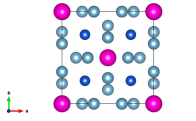
P2₁/m



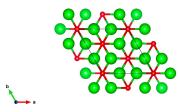
P2₁/m



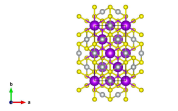
Eu(Al₂Cu)₄ (*I4/mmm*)



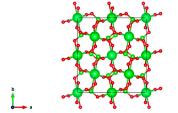
Zr₄O (*R $\bar{3}$*)



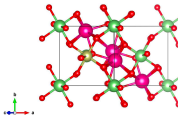
K₂Ni₃S₄ (*Fddd*)



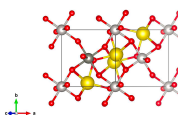
Sr(ClO₃)₂ (*Fdd2*)



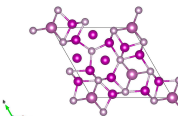
LiSm₂IrO₆ (*P2₁/c*)



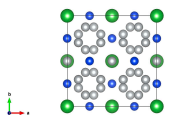
Pr₂ZnPtO₆ (*P2₁/c*)



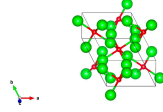
Sc₂Mn₁₂P₇ (*P $\bar{6}$*)



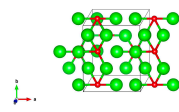
LaSi₂Ni₉ (*I4₁/amd*)



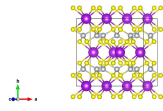
P $\bar{1}$



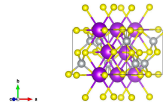
P1



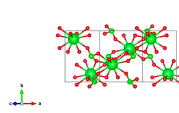
C2/m



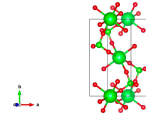
P2₁/c



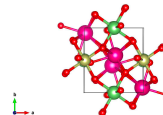
C2/c



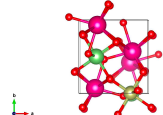
P2₁/c



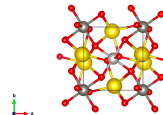
P2₁/n



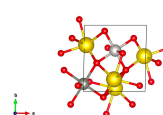
P2₁



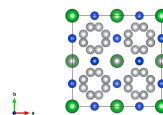
P2₁/n



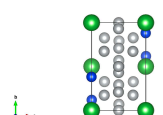
P1



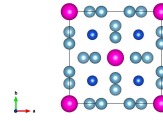
I4₁/amd



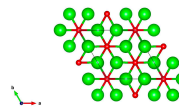
P2₁/c



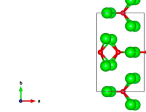
I4/mmm



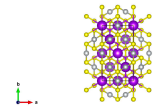
P $\bar{3}1m$



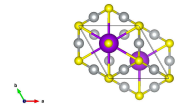
Pm



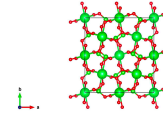
Fddd



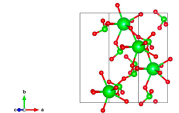
P6₃/mmc



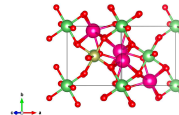
Fdd2



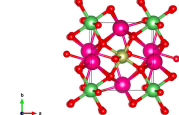
Cc



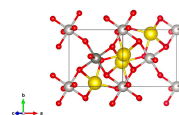
P2₁/c



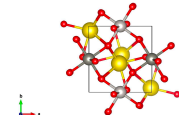
P $\bar{1}$



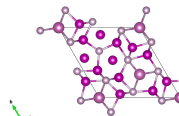
P2₁/c



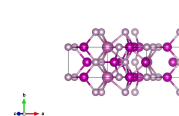
P $\bar{1}$



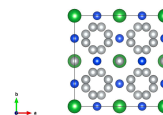
P $\bar{6}$

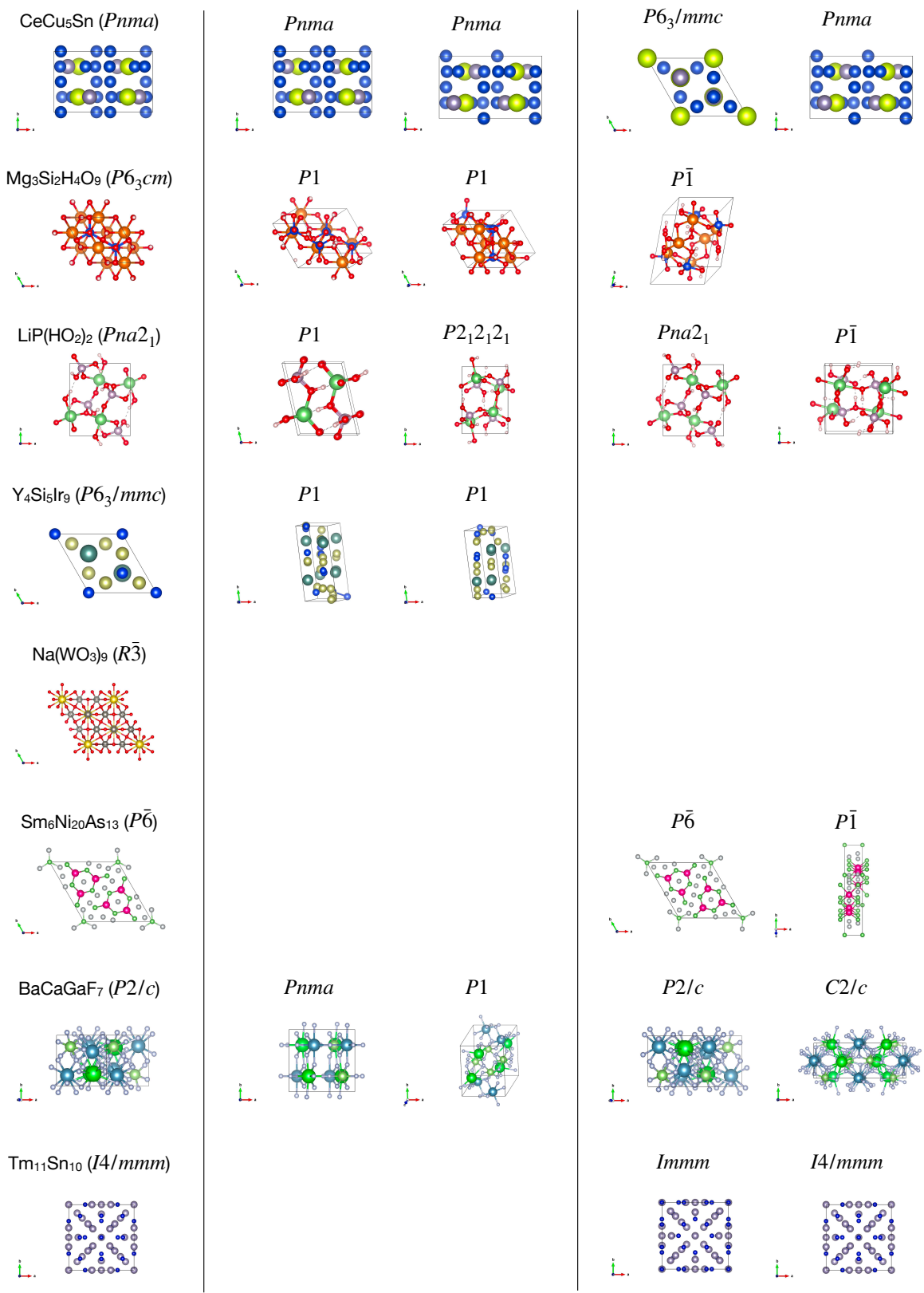


P6₃/mmc

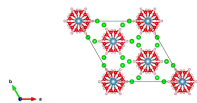


I4₁/amd

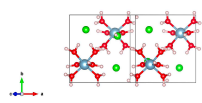




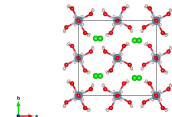
$\text{AlH}_{12}(\text{ClO}_2)_3$ ($R\bar{3}c$)



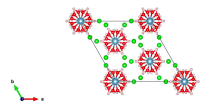
$P2_1/c$



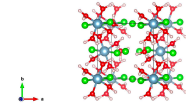
$Aea2$



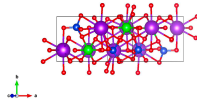
$R\bar{3}c$



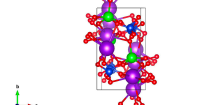
$P2_1/c$



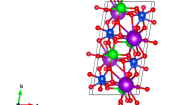
$\text{K}_2\text{ZrSi}_2\text{O}_7$ ($P2_1/c$)



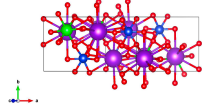
$P2_1/c$



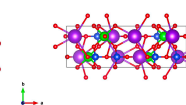
$P1$



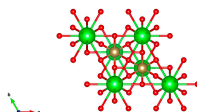
$P2_1/c$



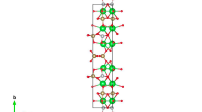
$Pnma$



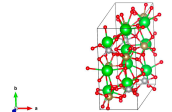
$\text{Ba}_3\text{Ta}_2\text{NiO}_9$ ($P\bar{3}m1$)



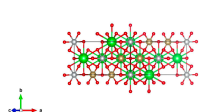
Pm



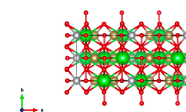
$P1$



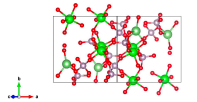
$P2_1/c$



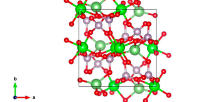
$P2_1/c$



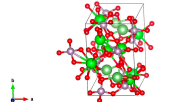
$\text{LiZr}_2(\text{PO}_4)_3$ ($P2_1/c$)



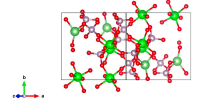
$Pna2_1$



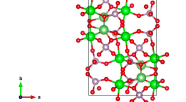
$P1$



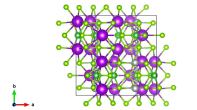
$P2_1/c$



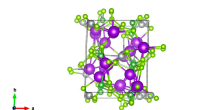
$P2_1/c$



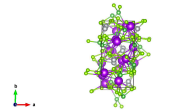
$\text{K}_5\text{Ag}_2(\text{AsSe}_3)_3$ ($Pnma$)



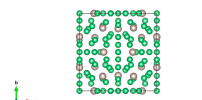
$P1$



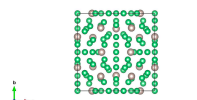
$P1$



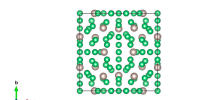
$Im\bar{3}$



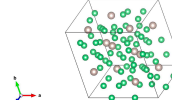
$\text{Be}_{17}\text{Ru}_3$ ($Im\bar{3}$)



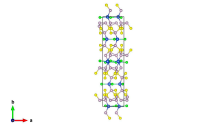
$Im\bar{3}$



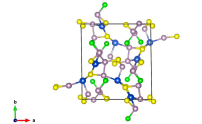
$P1$



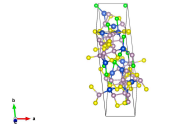
$\text{Cu}_3\text{P}_8(\text{S}_2\text{Cl})_3$ ($Pnma$)



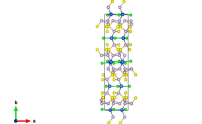
$P1$



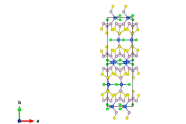
$P1$



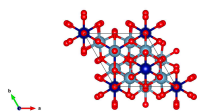
$Pnma$



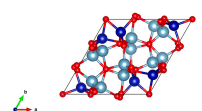
$Pnma$



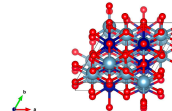
Al_2CoO_4 ($P3m1$)



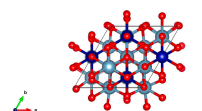
$P1$



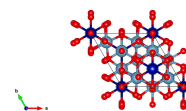
$P1$



$P1$



$P3m1$



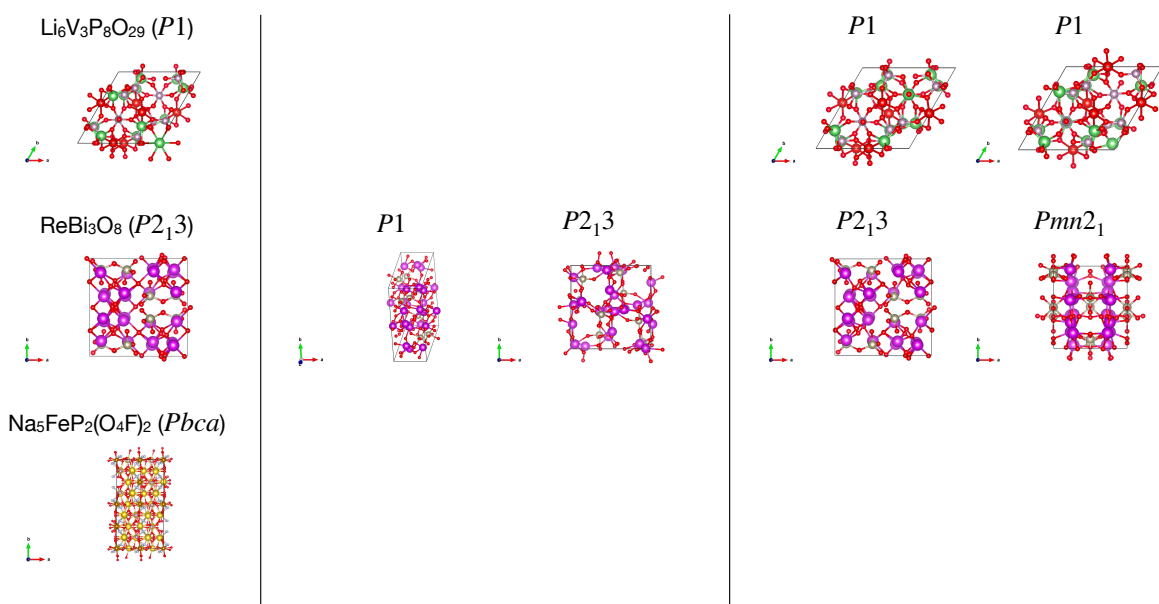


Figure S2. 90 stable structures solved by the crystal structure prediction algorithm (depicted with VESTA⁴⁹ version 3.5.8). For each prediction algorithm, the structures with the two lowest DFT energies are shown.